

KEEP CALM AND BARYON: THE DISTRIBUTION OF
BARYONS AND DARK MATTER ON COSMIC SCALES

BENJAMIN A. COOK

A SENIOR THESIS
PRESENTED TO THE FACULTY
OF PRINCETON UNIVERSITY
IN CANDIDACY FOR THE DEGREE
OF BACHELOR OF ARTS

RECOMMENDED FOR ACCEPTANCE
BY THE DEPARTMENT OF
ASTROPHYSICAL SCIENCES

ADVISOR: PROF. NETA BAHCALL

MAY 2014

I hereby declare that I am the sole author of this thesis.

I authorize Princeton University to lend this thesis to other institutions or individuals for the purpose of scholarly research.

Benjamin A. Cook

I further authorize Princeton University to reproduce this thesis by photocopying or by other means, in total or in part, at the request of other institutions or individuals for the purpose of scholarly research.

Benjamin A. Cook

Abstract

How are baryons distributed in the universe? Where, and in what abundances, are they located in large, virialized systems such as galaxies, groups, and clusters? Here we determine the distribution of baryons, relative to dark matter, in systems ranging in size from galaxies to groups, clusters, and large-scale structure. We use observed X-ray and SZ measurements of the hot intracluster medium (ICM) to determine the hot gas contribution in groups and clusters; weak lensing and optical constraints on the cluster stellar fraction; and absorption measurements of the cool circumgalactic medium (CGM) to determine the gas mass in galaxies. Using direct observations when possible, and extrapolations of observed density profiles when necessary, we show that the baryon content within the virial radius is consistent with the cosmic baryon fraction (0.164 ± 0.004) for systems ranging over three orders of magnitude in mass, from galaxies to groups and massive clusters. The baryon distribution is less extended in massive systems and more broadly distributed in low-mass systems. Averaged on scales larger than the virial radius, the baryonic mass is a strong tracer of the underlying dark matter distribution, and the dark matter, stellar, and gaseous components of groups, clusters, and large-scale structure may be comprised only of the contributions from the individual constituent galaxies of these larger systems. Baryons, which initially fell into the gravitational potentials formed by dark matter, have not been removed significantly from these systems, but remain in roughly the cosmic fraction in galaxies, groups, clusters, and large-scale structure.

Acknowledgements

First and foremost, I would like to thank Neta Bahcall for her wonderful support and guidance throughout this project, my graduate application process, and my entire Princeton career. She is an inspiration and invaluable mentor to every student in astrophysics and made me feel welcome in the department from my first day on campus. I'm very glad to have gotten the chance to conclude my senior year by working with her on this project, and I look forward to collaborating more on it in the future. I would like to thank Professor J. Xavier Prochaska, Professor Lars Hernquist, and Dr. Shy Genel for their discussions and insight into their work. I would also like to thank Dr. Renyue Cen for making his simulations available for my analysis, which I regret I was not able to include in this thesis. Thank you to Tomer, Michael, Fred, and all the astro undergrads for the great times studying and working together in Peyton. Thank you to Shelby for believing in me, for giving me a reason to try harder and reach my full potential, and for always lifting my spirits when work is overwhelming. Finally, I would like to thank my parents, Kelly and Tom, for their love and encouragement and for giving me the opportunity to make it where I am today.

Dedicated to my brother, Walter.

I'm very proud of you, and know you will accomplish amazing things.
Continue to challenge yourself, and I'll enjoy my headstart while it lasts.

Contents

Abstract	iii
Acknowledgments	iv
1 Introduction	1
1.1 The Matter and Energy Components of the Universe	1
1.2 The Cosmic Baryon Fraction	2
1.3 The Cluster Missing Baryon Problem	9
1.4 The Galaxy Missing Baryon Problem	15
1.5 Our Investigation – Where are the Baryons?	16
2 Observations and Data Analysis	19
2.1 Total Mass in Groups and Clusters	19
2.2 Group and Cluster Gas Mass Fractions	21
2.2.1 Observations	22
2.2.2 Extrapolation of Gas Density Profiles	27
2.3 Group and Cluster Stellar Mass Fractions	30
2.4 Galaxy Mass Fractions	32
2.4.1 The Circumgalactic Medium	34
2.4.2 Estimate of The Galactic Baryon Fraction	36
3 Results	39
3.1 The Distribution of Gas, Stars, and Baryons in Groups and Clusters .	39

3.2	The Baryonic Content of Systems from Galaxies to Groups and Clusters	45
4	Discussion	48
4.1	Limitations and Observational Biases	48
4.1.1	The Hydrostatic Mass Bias	48
4.1.2	The Gas Clumping Bias	50
4.1.3	Extrapolation of the Density Profile Slope	52
4.2	Comparison to Simulations	53
4.3	Implications	56
4.3.1	Deviations from Self-Similarity	57
4.3.2	The Contribution of Individual Galaxies to Clusters	58
4.3.3	Where are the Baryons?	60
5	Summary and Conclusions	62
	Bibliography	71

Chapter 1

Introduction

1.1 The Matter and Energy Components of the Universe

After the big bang, the energy content of the universe was distributed in a diverse number of components. As the universe expanded and cooled, the available energy settled down into the primary forms we observe today, including radiation (photons and neutrinos), baryons (“ordinary” matter, comprised of protons, neutrons, and electrons), as well as the mysterious dark matter and dark energy.

Energy did not populate these forms in equal proportions; the energy densities of each component differed by many orders of magnitude, initially, and their ratios have changed continually throughout the expansion history of the universe. Radiation density – primarily the photon density (ρ_γ), dominant in the earliest periods after the big bang – diluted quickly from the combination of expansionary volume increase and Doppler redshifting. The matter density – ρ_m , comprised of both baryons (ρ_b) and cold dark matter (ρ_c) – was initially only a minuscule portion of the cosmic energy budget, but eventually matter dominated the cosmic scene after expansion cooled the photon temperature significantly. Initially insignificant relative to the energy content

of the other components, dark energy – ρ_Λ , commonly thought to be a cosmological constant Λ – retains a constant energy density while the universe expands and became dominant at late times when ρ_m had decreased significantly. Each of these energy densities are often scaled by the critical density required to stop cosmic expansion:

$$\rho_{crit} = \frac{3H^2}{8\pi G} \quad (1.1)$$

with H the Hubble parameter and G Newton’s constant. The density of each component relative to the critical density is expressed as Ω . For example:

$$\frac{\rho_b}{\rho_{crit}} = \Omega_b . \quad (1.2)$$

1.2 The Cosmic Baryon Fraction

Baryons and dark matter, the two components of the total matter density, have the same dependence on the expansionary scale factor and redshift. Since the total matter density is just their sum, the total matter density also scales identically:

$$\begin{aligned} \rho_c \propto \rho_b \propto \rho_m \propto a^{-3} \\ \propto (1+z)^3 . \end{aligned} \quad (1.3)$$

Therefore, we see that the ratio of baryons to dark matter will remain constant at its primordial level throughout the history of the universe. A useful and commonly studied constant is the *cosmic baryon fraction*, f_b , the fraction of all matter in baryonic form:

$$f_b = \frac{\rho_b}{\rho_b + \rho_c} = \frac{\rho_b}{\rho_m} = \frac{\Omega_b}{\Omega_m} . \quad (1.4)$$

The above argument, that the baryon fraction remains constant throughout cosmic history, applies only in the homogeneous regime, when there are no spatial variations

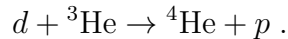
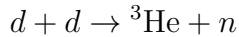
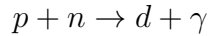
in the overall mass density. If inhomogeneities exist, self-interactions lead to the complicated evolution of structure. While dark matter (by energy density) dominates the gravitational collapse of inhomogeneities and drives the growth of structure, it is obvious that the baryon abundance plays an incredibly important role in determining the makeup of our universe. Dark matter interacts only through gravity, but baryons are subject to electromagnetic forces, thermal emission, collisions, and numerous other interactions collectively known as “baryonic physics”. Baryons are solely responsible for all non-gravitational phenomena studied in physics and astrophysics: the formation of galaxies, stars, and planets, supernovae, radiation, magnetism, chemistry, and, eventually, life itself.

Initially, baryons fall into the gravitational potentials made by dark matter (known as “dark matter halos”) in a proportion equal to the cosmic baryon fraction. Over time, the baryonic gas cools, forming stars and galaxies, and baryonic physics can drive dramatic changes in the distribution of baryons relative to dark matter. Halos are initially populated by the cosmic fraction of baryons, but mechanisms such as shock heating, galactic winds, or AGN activity could drive baryons out of the potential well altogether, leaving systems deficient of baryons relative to the cosmic fraction. Although the local baryon fraction may vary within different regions of virialized systems, it is possible to estimate the baryon fraction in these systems by averaging over a substantially large volume. By studying the baryon fraction (and what forms the baryons take) we can learn about the relative distributions of dark matter and baryons, and the contributions of baryonic and gravitational physics to the formation of structure.

The baryon and dark matter abundances were major factors in several important physical processes in the early universe. Through observable signatures of these processes, cosmologists have been able to place powerful constraints on the cosmic baryon fraction at these early times. Consistent with the literature, we will consider

the baryon fraction inferred from these methods to be the cosmic fraction against which we will compare measurements from the local, highly inhomogeneous universe.

One mechanism that constrains the baryonic abundance is big bang nucleosynthesis (BBN), the process which generated the first light elements beyond hydrogen¹. In the first seconds after the big bang, the only ordinary matter particles which existed (and were stable) were protons (p), electrons (e), neutrons (n), and deuterium (d). The high temperatures and densities of nucleons allowed the conversion of protons and neutrons into more complex and heavier nuclei, through processes such as:



The BBN reactions began around 100 – 200 seconds after the big bang (Weinberg, 2008). The exact time when these reactions reached thermal equilibrium depends weakly on the abundance of baryons, $\Omega_b h^2$, where $H_0 = 100h \text{ km s}^{-1} \text{ Mpc}^{-1}$ defines h , an important scaling factor². After the universe expanded and cooled sufficiently, these reactions fell out of equilibrium, leaving the universe enriched with helium (${}^4\text{He}$ and ${}^3\text{He}$) and trace amounts of elements such as deuterium and lithium (${}^7\text{Li}$). The higher $\Omega_b h^2$, the more complete the transformation of n and d into helium. Therefore, the baryon abundance strongly affects the resulting abundance of deuterium and residual elements like lithium and ${}^3\text{He}$. Figure 1.1 shows the dependence of these primordial abundances on the cosmic baryon abundance.

The baryon abundance can be determined through observational constraints of,

¹The discussion which follows is guided primarily by Chapter 3.2 of Weinberg (2008), a useful but relatively technical reference on the topic.

²Uncertainties on the true expansion rate (h) translate into uncertainties on a number of observables such as matter abundances (Ω) and dark matter halo properties (M or r). Therefore, many derived properties in the literature are often given in terms of $h_{70} \equiv H_0/70 \text{ km s}^{-1} \text{ Mpc}^{-1}$.

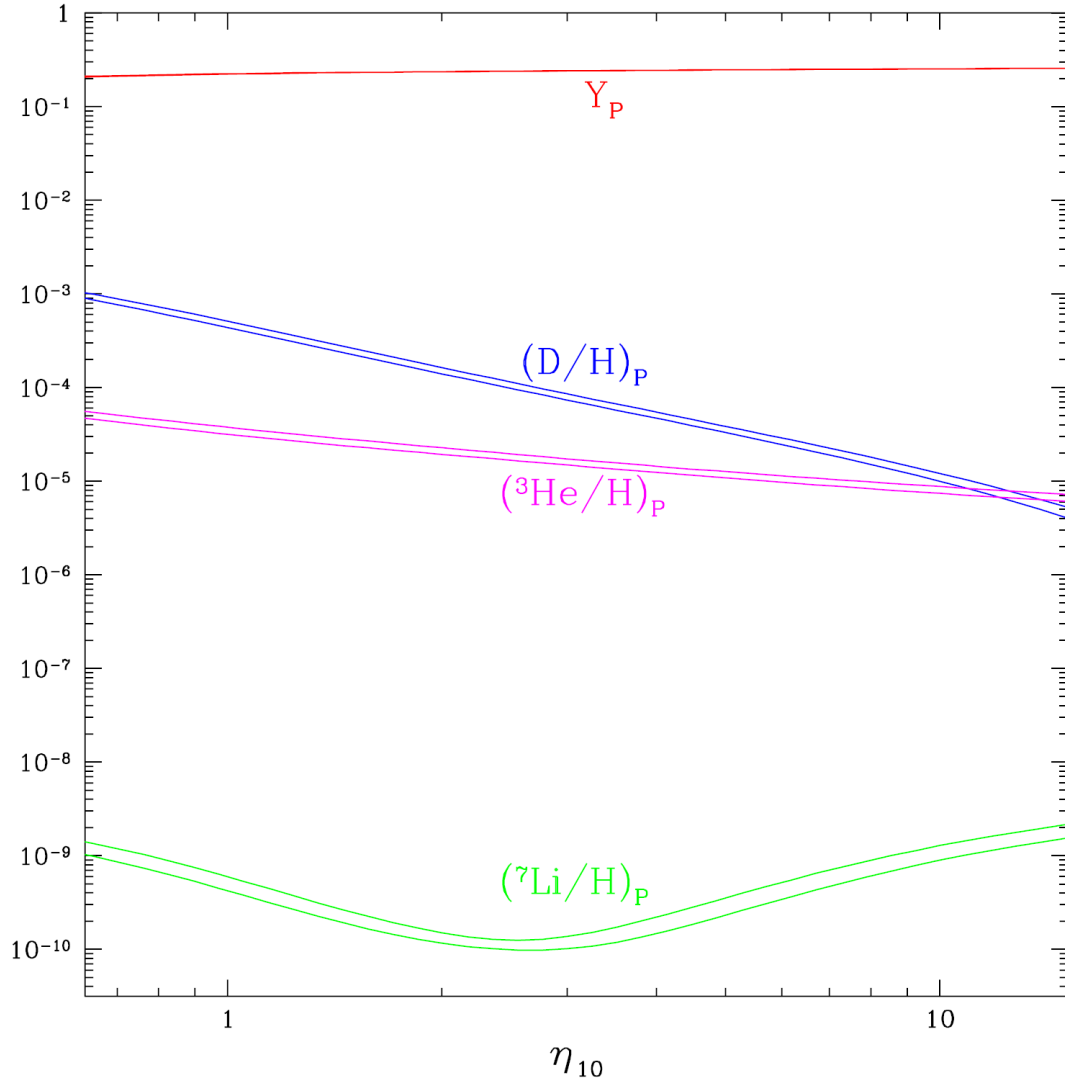


Figure 1.1: The BBN-predicted primordial abundances of deuterium (D), ${}^3\text{He}$, ${}^7\text{Li}$, and ${}^4\text{He}$ (Y_P), as a function of the baryon abundance parameter $\eta_{10} \sim 274 \times \Omega_b h^2$. The width of the curves represents the uncertainties in various nuclear reaction rates. Figure taken from Steigman (2006, Fig. 1), another helpful overview of BBN physics.

for example, the deuterium abundance, which among the byproducts of BBN depends most strongly on $\Omega_b h^2$. The deuterium abundance has been inferred from variety of sources, including from the Milky Way’s ISM (Linsky et al., 1993, 1995), absorption towards QSOs (Tytler et al., 1996; Kirkman et al., 2003), and even from measurements of the composition of the Jovian atmosphere (Niemann et al., 1996). All such methods have limitations, as deuterium can be destroyed in stellar (and brown dwarf) cores, altering the deuterium abundance slightly with time. Iocco et al. (2009) provides a compilation of deuterium abundance measurements, placing a constraint on the baryon abundance of $\Omega_b h^2 = 0.021 \pm 0.001$. Observed ${}^7\text{Li}$ abundances are a factor of a few lower than predicted from BBN, suggesting that there could be additional physics responsible for destroying lithium (Suzuki et al., 2000; Meléndez & Ramírez, 2004). This is known as the “Lithium Problem,” and is still an unsolved problem in interpreting BBN.

A complementary method of inferring the baryon abundance at early times is from measurements of the acoustic peaks in the Cosmic Microwave Background (CMB) fluctuations power spectrum. The CMB power spectrum contains large peaks, representing correlations in the CMB on particular scales. In the first few hundred thousand years after the big bang, the temperature of the universe was high enough to keep atoms fully ionized into separate nuclei and electrons. These charged particles were strongly coupled to the local photon field through Thompson Scattering, so that the two components combined to form what is called a photon-baryon fluid. This fluid fell towards the centers of gravitational wells created by dark matter. However, unlike the non-interacting dark matter, the photon-baryon fluid’s pressure rose when the density rose, stopping its infall. The pressure build-up forced the fluid back out of the well until its pressure dropped enough to allow gravity to draw it back in once again. These ongoing fluctuations in the pressure and density of the fluid were frozen into the CMB power spectrum as the acoustic peaks. This occurred when the aver-

age temperature of the universe dropped sufficiently to allow neutral atoms to form, and the CMB photons began streaming freely through the universe, around redshift $z = 1100$, when the universe’s average temperature was $T \approx 3000\text{K}$ ³.

The baryon abundance at this early time had several effects on the acoustic peaks in the CMB, as did the cold dark matter abundance ($\Omega_c h^2$). Figure 1.2 shows how changes in these abundances are reflected in the acoustic peaks. The location of the first peak (and all subsequent peaks) is determined by the sound speed at the epoch of last scattering. This sound speed decreases when $\Omega_b h^2$ increases (Mukhanov, 2005, ch. 9.8). The total curvature of the universe (determined primarily at this time by $\Omega_c h^2$) also shifts the location of each peak. The relative heights of the acoustic peaks is a further diagnostic of the baryon abundance. As seen in Figure 1.2, odd-numbered peaks are higher than even-numbered peaks in a universe with high $\Omega_b h^2$. This is because an increase in the amount of massive baryons reduces the frequency of acoustic oscillations (Dodelson, 2003, ch. 8.7.3). High $\Omega_c h^2$ decreases the overall height of each peak. Finally, the power spectrum declines towards higher multipoles (l) due to a process known as “Silk Damping”. This damping term is due to imperfections in the photon-baryon coupling, and the characteristic damping scale is influenced by $\Omega_b h^2$ (Durrer, 2008, ch. 4.7).

Through a combination of all the processes listed above, modern CMB observations have been able to place strong constraints on both $\Omega_b h^2$ and $\Omega_c h^2$. Two of the most noteworthy such measurements come from the *Wilkinson Microwave Anisotropy Probe* (*WMAP*, Bennett et al., 2003) and the *Planck* Satellite (Planck Collaboration, 2013a). Different constraints are placed on these parameters depending on what additional data⁴ is included in the analysis. We will use the median value (from each paper) of parameters derived through these various methods, and we use the system-

³For an introductory discussion on the concept of acoustic peaks in the CMB, see Chapter 9 of Ryden (2003).

⁴ H_0 , BAO, polarization, etc.

atic variance in the parameters as the uncertainty, if it is larger than the statistical uncertainty listed from the analysis.

From the 9-year data release of *WMAP* (*WMAP*9, Hinshaw et al., 2013), we use $\Omega_b h^2 = 0.02229 \pm 0.00035$ and $\Omega_c h^2 = 0.1138 \pm 0.0032$. From the results paper of *Planck* (Planck Collaboration, 2013b), we use $\Omega_b h^2 = 0.022115 \pm 0.00025$ and $\Omega_c h^2 = 0.11957 \pm 0.0025$. These values allow us to constrain the cosmic baryon fraction as:

$$\begin{aligned} f_b &= \frac{\Omega_b h^2}{\Omega_b h^2 + \Omega_c h^2} \\ &= 0.164 \pm 0.004 \text{ (} WMAP9 \text{)} \\ &= 0.156 \pm 0.003 \text{ (} Planck \text{)} \end{aligned} \tag{1.5}$$

The uncertainty on f_b comes from the propagation of uncertainties on $\Omega_b h^2$ and $\Omega_c h^2$:

$$\begin{aligned} \Delta f_b &= \sqrt{\left(\frac{\partial f_b}{\partial \Omega_b h^2}\right)^2 \Delta(\Omega_b h^2)^2 + \left(\frac{\partial f_b}{\partial \Omega_c h^2}\right)^2 \Delta(\Omega_c h^2)^2} \\ &= \sqrt{\left(\frac{\Omega_c h^2 \Delta(\Omega_b h^2)}{(\Omega_b h^2 + \Omega_c h^2)^2}\right)^2 + \left(\frac{\Omega_b h^2 \Delta(\Omega_c h^2)}{(\Omega_b h^2 + \Omega_c h^2)^2}\right)^2} \\ &= \frac{1}{(\Omega_m h^2)^2} \sqrt{[\Omega_c h^2 \Delta(\Omega_b h^2)]^2 + [\Omega_b h^2 \Delta(\Omega_c h^2)]^2} \end{aligned} \tag{1.6}$$

It is commonly discussed (e.g., Spergel et al., 2013) that the *Planck* results yield Ω_m significantly higher and H_0 significantly lower than other previous measurements, including *WMAP*. This results in the lower value of f_b as derived from *Planck*. Earlier estimates (e.g., *WMAP*5, Dunkley et al., 2009) placed f_b around 0.17, a canonical value which is often used in the literature. Here, we will use the *WMAP*9 measurement of $f_b \sim 0.164$ for our primary comparisons with low-redshift baryon fractions, although we will attempt to also compare to the *Planck* constraints whenever possible. One limitation of this work is the relative uncertainty on the “cosmic” baryon fraction

due to the discrepancies in CMB observations. We hope that subsequent analysis will resolve this problem.

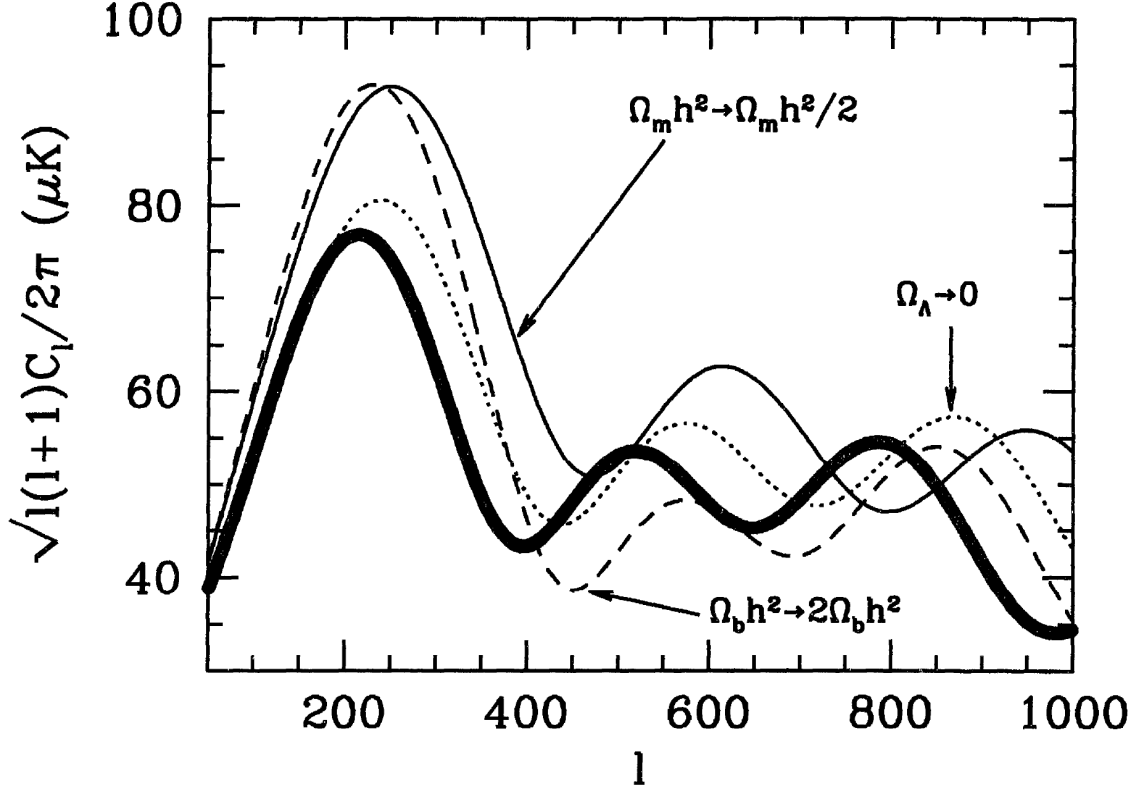


Figure 1.2: The variation in the CMB power spectrum's acoustic peaks due to variations in cosmic abundance parameters. The thick black line represents a fiducial universe with $\Omega_m h^2 = 0.16$, $\Omega_b h^2 = 0.021$, and $\Omega_\Lambda = 0.7$. Other lines represent the results from changes to these parameters, notably an increase in peak height and rightward shift of peaks ($\Delta l > 0$) with an increase in $\Omega_b h^2$. A decrease in $\Omega_m h^2$ has similar (but distinguishable) effects. Figure from Dodelson (2003, Fig. 8.19).

1.3 The Cluster Missing Baryon Problem

Large *galaxy clusters* represent the most massive dark matter systems which have had adequate time to virialize since the big bang. The richest clusters often contain hundreds of large galaxies, while much smaller *groups* may contain several to tens of galaxies. The galaxies are bound to the gravitational well of the combined mass

of the cluster, which includes dark matter as well as baryons. Some clusters show a steep pressure profile (and a flat density profile) towards their centers, suggesting that they are dynamically *relaxed* and possess a *cool core* (these are known as cool core or CC clusters). Clusters with flattened central pressure profiles (and cuspy density profiles) are *unrelaxed* or *non-cool core* (NCC) clusters. Because they are the largest bound objects in the universe, clusters offer one of the best ways of measuring the baryon fraction at low-redshift: they have collapsed from large volumes ($\sim 8 h^{-1}$ Mpc in radius) and therefore represent the largest samples of the cosmic dark matter and baryon densities that are not in dramatic dynamical evolution. Additionally, their deep gravitational potential wells are expected to prevent any significant fraction of baryons from escaping the system through feedback effects, such as winds, supernovae, or AGN activity.

The baryonic component of groups and clusters is not primarily stored in galaxies, but in a hot ($kT \gtrsim 1$ keV), diffuse gas known as the *Intracluster Medium* (ICM). The ICM can be detected through the X-ray Brehmsstrahlung emission of the ionized plasma. X-ray telescopes such as *Chandra*, *ROSAT*, *Suzaku*, and *XMM-Newton* have been key in detecting the ICM and constraining its distribution and total mass (e.g., Vikhlinin et al., 2006; Eckert et al., 2012). A complementary method of detecting and measuring the intracluster gas is through the thermal Sunyaev-Zeldovich effect (SZ, Sunyaev & Zeldovich, 1972), which occurs when the energy spectrum of background CMB photons passing through the cluster is altered due to inverse-Compton scattering with the charged particles in the plasma.

The stars of individual galaxies make up the remainder of the baryonic mass in groups and clusters. Stellar mass is derived from the luminosity in starlight, which is converted into mass using the observed colors or spectra of galaxies, or from the typical stellar mass to light ratios derived for individual galaxies (Bahcall & Kuier, 2014).

The total mass of groups and clusters is derived through stacked weak-lensing analysis, where the average distortion of background galaxies is measured as a function of cluster-centric radius. These distortions can be inverted to compute the distribution of mass in the cluster which is responsible for the gravitational lensing distortions. Recent weak-lensing analyses (Mandelbaum et al., 2008; Sheldon et al., 2009a) yield accurate constraints on the total mass of clusters, and show that the distribution of mass is fit well by the Navarro-Frenk-White profile (NFW, Navarro et al., 1996), a prediction from N-body simulations of cold dark matter.

Before addressing the overall masses and sizes of galaxy clusters, it is important to outline the definitions for these scales we will use throughout this paper. Because dark matter halos are believed to be self-similar (scaling only by overall mass or central density) their sizes are often given relative to fixed overdensities Δ , the location where the density of matter interior is a particular multiple of the critical density of the universe. For example, $\Delta = 200$ equates to the region in a system where

$$\rho_m(< r) = \frac{3M(< r)}{4\pi r^3} = 200 \times \rho_{crit} . \quad (1.7)$$

The mass and radius of a group or cluster is typically measured at a characteristic overdensity. For example, many sources in the literature list the group and cluster mass and radius as M_{500} and r_{500} , measured at an overdensity of $\Delta = 500$. As cluster mass-density increases towards the center, Δ decreases towards larger cluster-centric radii. The gravitational system virializes around $\Delta = 100$ in the Λ CDM cosmology (Eke et al., 1996), so we take the characteristic scales of groups and clusters to be the virial mass and radius, $M_{vir} \equiv M_{100}$ and $r_{vir} \equiv r_{100}$.

Through stacked weak lensing measurements, rich galaxy clusters have been observed to have virial masses of $10^{14} - 10^{15} M_{\odot}$ (Mandelbaum et al., 2008), and virial radii of around $1 - 3$ Mpc (Vikhlinin et al., 2006). Lower-mass groups typically have

masses around $10^{13} - 10^{14} M_{\odot}$, and represent the intermediate range between the most massive clusters and large galaxies. The self-similarity of group and cluster halos results in a fairly constant relation between masses or radii at various overdensities. For example (Rasheed et al., 2011):

$$r_{vir} \approx 1.3 \times r_{200} \approx 1.9 \times r_{500}. \quad (1.8)$$

Using an approximate mass density profile of $\rho_m \propto r^{-2.5}$ in these outer cluster regions, we assume that the total mass scales roughly as $M \propto r^{0.5}$, so that

$$M_{vir} \approx 1.14 \times M_{200} \approx 1.38 \times M_{500}. \quad (1.9)$$

Recent X-ray and SZ measurements have begun to illuminate the hot intracluster plasma, allowing detailed study of these large reservoirs of baryons in groups and clusters. X-ray surface brightness observations, in particular, are able to directly measure the gas density profile and therefore retrieve the mass. However, because Brehmsstrahlung emission declines with the square of the gas density, accurate X-ray measurements have typically been limited to the inner regions of groups and clusters. Studies of this kind in clusters include Vikhlinin et al. (2006, with *Chandra*) and Arnaud et al. (2007, with *XMM-Newton*), while Sun et al. (2009) made similar measurements of the hot gas in groups using *Chandra*. Measuring the gas mass fraction (the internal gas mass divided by the total mass) only out to r_{500} , these observations typically found $f_{gas}(< r_{500}) \approx 6 - 12\%$, well below the cosmic baryon fraction, although with large variance between clusters. Importantly, there is a clear trend towards lower gas content in lower-mass groups, which show gas fractions below 10% at r_{500} . The stellar fraction in clusters has been observed to increase in smaller groups (Giodini et al., 2009; Bahcall & Kulier, 2014). However, stars make up only a few percent of the total mass even in groups, and represent $< 2\%$ of the total

mass budget within r_{500} in rich clusters. Combining the ICM gas and stellar mass within r_{500} , there is not enough baryonic matter to make up the total baryon content expected from the cosmic fraction.

These discrepancies have been termed the “Missing Baryon Problem”, (Figure 1.3) because observations have not been able to account for the expected abundance of baryons in galaxy clusters. The problem is more severe in smaller clusters, likely because baryons are less strongly bound to their shallow gravitational wells. Many attempts have been made to find a solution to this problem through theoretical and computational means. Possibly the most predominant such explanation is that additional non-gravitational energy is injected into the cluster, such as through shocks (Takizawa & Mineshige, 1998), preheating (Bialek et al., 2001), or a number of feedback mechanisms due to star formation or AGN activity (Metzler & Evrard, 1994; McCarthy et al., 2007; Bode et al., 2009). The net result of these additional energy sources is to extend the distribution of hot gas in the ICM, pushing more gas into the outskirts of the clusters while leaving the central regions deficient in gas. These theories predict that more sensitive analysis of the outskirts of groups and clusters ($\sim r_{vir}$) should recover the missing gas mass left unaccounted for by observations of only the inner cluster regions. Rasheed et al. (2011) used extrapolations of observed gas density profiles to r_{vir} , showing that the missing gas mass is indeed located in the outskirts of groups and clusters. Alternative theories predict that the missing baryons could be residing in additional phases, such as a cool diffuse gas phase, that have yet to be identified observationally (Afshordi et al., 2007; Bonamente et al., 2005).

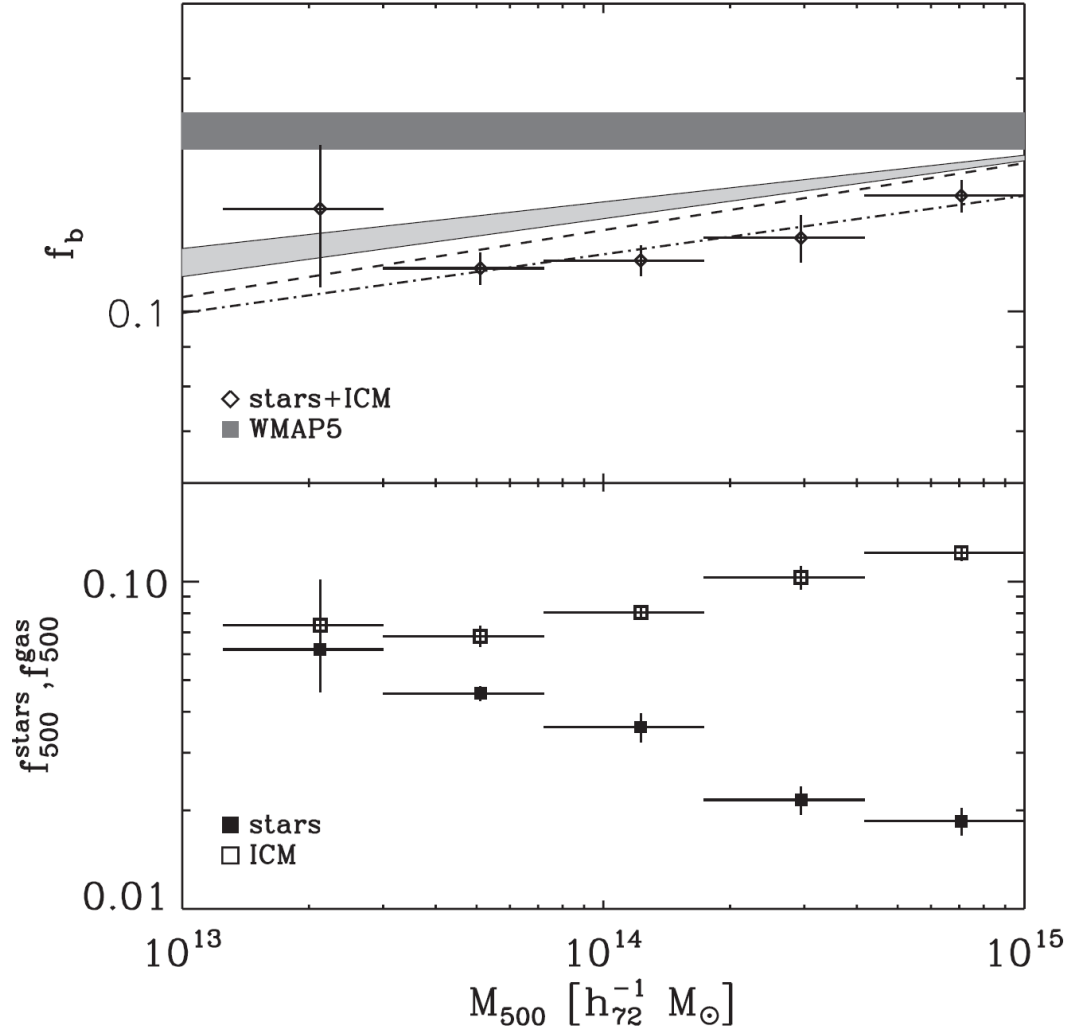


Figure 1.3: The problem of missing baryons, relative to mass, in groups and clusters. *Upper:* shows the total baryon fraction within r_{500} for groups and clusters binned by mass. The dark grey stripe represents the cosmic baryon fraction. All clusters are short of baryons, but low-mass systems are particularly deficient. *Lower:* the gas and stellar fractions of the mass bins. Figure from Giodini et al. (2009).

1.4 The Galaxy Missing Baryon Problem

Galaxies form in dark matter halos of a range of sizes. Galaxies like the Milky Way and Andromeda (near the high-end of the galaxy mass range) are commonly referred to as L^* galaxies, and typically reside in systems with total mass upwards of $10^{12} M_{\odot}$ (Moster et al., 2010). The virial radii of these systems are around 300 kpc (Werk et al., 2014, and refs. therein). The baryonic components which dominate the energy output in these systems (and are therefore the easiest to detect through emission) include the stellar disk, the gas and dust of the interstellar medium (ISM), and a hot, X-ray emitting halo of gas. Yet the most recent estimates of stellar mass in L^* galaxies (Behroozi et al., 2010) find that the stellar component makes up only $\approx 5\%$ of the total mass, far less than anticipated if galactic systems also contain the cosmic baryon fraction. Including the cold ISM gas measured by HI surveys and the hot X-ray halo (Martin et al., 2010; Gupta et al., 2012, respectively) only increases the estimated baryon fraction in galaxies to around 8%. Therefore a similar “Missing Baryon Problem” is discussed in galactic halos because observations cannot account for the entire anticipated baryon mass.

Several models have been developed which attempt to solve this “Galaxy Missing Baryon Problem,” through, for example, gas escaping galaxies through winds, jets, and outflows. Some theories predict unseen components in the intergalactic medium (IGM) which act as further reservoirs for baryons, but have yet to be accurately measured. These intergalactic components include a highly-photoionized $\text{Ly}\alpha$ forest (Sargent et al., 1980; Cen et al., 1994) or the warm-hot intergalactic medium (WHIM Cen & Ostriker, 1999; Dave et al., 1999).

One additional reservoir for galactic baryons, however, is a diffuse region of gas within the galactic dark matter halo itself, known as the circumgalactic medium (CGM, first suggested by Bahcall & Spitzer, 1969; Bergeron, 1985; Lanzetta et al., 1995), which may contain a large mass of baryons. Observationalists have begun to

probe the CGM in the last few years through studies of QSO or galactic sightlines which pass through the CGM of foreground galaxies (Steidel et al., 2010; Prochaska et al., 2011; Tumlinson et al., 2011; Werk et al., 2013). When photons emitted by the background quasar or galaxy pass through the CGM of the nearby galaxy, the gas (not energetic enough to be detected in emission) absorbs characteristic spectral lines from the background spectrum, depending on the chemical makeup of the gas. The most common lines observed in absorption come from neutral hydrogen – hydrogen being the dominant source of baryonic mass in the universe. However, absorption from more highly-ionized species, such as Ca II (Zhu & Ménard, 2013), Mg II, Si II, C II, and O VI (Tumlinson et al., 2011; Werk et al., 2014), which are not significant contributors to baryonic mass, can be used to characterize the ionization state of the CGM gas.

Knowledge of the ionization state can constrain the total hydrogen mass, including both neutral H I gas and the ionized H II. The observed metal-line absorption in QSO sightlines and the enrichment of the CGM also suggest that feedback effects are substantial in galactic systems: metals created in the stellar disk are expelled into the outer regions of the galactic system, or even lost altogether, by feedback winds of $\gtrsim 10^2 \text{ km s}^{-1}$ (D’Odorico & Savaglio, 1991; Chen et al., 2010; Oppenheimer et al., 2012; Booth et al., 2012). New observations by the COS-Halos project show that the galaxy CGM indeed contains a significant amount of extended gas (out to the virial radius of 300 kpc) that could dramatically increase the baryon fraction observed in galactic systems.

1.5 Our Investigation – Where are the Baryons?

In this thesis, we examine the most up-to-date observations available that can address the overall distribution of baryons relative to dark matter. Previous works have

focused on the narrow question of the “Missing Baryon Problems” described above, and this question is starting to be answered. Generally, we wish to consider the larger issues of the overall distribution and history of baryons in dark matter potentials. This thesis addresses the questions: where are the baryons in the universe, what forms are they in, and how are they correlated with dark matter halos of all sizes?

Gas density profiles in groups and clusters are observed to be shallower than the dark matter (NFW) profile, suggesting that there should be large reservoirs of baryons in the outskirts (e.g., Rasheed et al., 2011). We use published SZ and X-ray observations of cluster outskirts – along with extrapolations of the inner density profiles when necessary – to show that groups and clusters *do contain the expected baryon gas fraction* when integrated to approximately their virial radius. The baryons which originally fell into groups and clusters have not been ejected from the potential, and nearly the entire cosmic fraction of baryons remains within the systems.

Galaxies have significantly lower mass than clusters and their binding potential is lower, making it easier to expel baryons from the galaxy by feedback effects. Because of this, it is possible that the “Galaxy Missing Baryon Problem” is a consequence of a majority of baryons being removed from the galaxies altogether. However, the new observations of the CGM allow powerful constraints of the mass-content of the outer galactic regions. We study the distribution of baryons in galaxies using available absorption measurements of the CGM, and find the galaxy baryon fraction may in fact be consistent with the cosmic baryon fraction; a large fraction of the baryons simply reside in the hard-to-detect CGM. Including the gas mass of the CGM with the stellar disk and ISM, we suggest that nearly the entire cosmic fraction of baryons has also remained within galactic potentials.

Our investigation is organized as follows. In Chapter 2, we present the observations which constrain the baryonic mass within galaxies, groups, and clusters. We also discuss the ways in which we determine the baryon fraction at the virial radius from

extrapolations of measurements in the more central regions. In Chapter 3, we show our results and compare the observed baryon fraction in galaxies, groups, and clusters to the cosmic baryon fraction derived from BBN and the CMB. We demonstrate that current evidence suggests that, averaged over sufficiently large scales of $\sim r_{vir}$, all systems contain baryons in abundances consistent with the cosmic baryon fraction. This is observed in a wide range of system sizes, from galaxies to groups and clusters and large-scale structure. In Chapter 4, we discuss the observational limitations and potential biases of our findings, compare them to simulations, and discuss the implications of our results. In Chapter 5, we present our conclusions on the subject of the baryonic mass distribution, and highlight future work that can be done to improve our findings.

Throughout this paper, we assume a cosmology of $\Omega_m = 0.3$, $\Omega_\Lambda = 0.7$, $H_0 = 70 \text{ km s}^{-1} \text{ Mpc}^{-1}$ ($h = 0.7$). Subscripts typically signify the value is evaluated within the indicated radius, such as $f_{gas,500} = f_{gas}(< r_{500})$. The “virial” mass and radius are defined to be at $\Delta = 100$. We adopt the term “halo” to refer generically to gravitationally bound systems of dark matter and baryons, which can take on a range of sizes from “galaxy halos” to “group halos” or “cluster halos”.

Chapter 2

Observations and Data Analysis

2.1 Total Mass in Groups and Clusters

The total mass in groups and clusters can be measured in a number of ways. The most direct method of determining the mass profile of a large halo is through gravitational lensing of the light of background sources behind the halo. Strong gravitational lensing occurs when the background object (e.g., a high-redshift galaxy) is magnified and severely warped by the gravitational potential of the lens (foreground cluster). This allows a very accurate measurement of the mass of the lens within the lensed arc radius, but occurs only rarely when the background/foreground are aligned, and it provides the mass only within the inner strongly lensed region. More commonly utilized to obtain the mass to larger radius is the technique of weak gravitational lensing (e.g., Umetsu et al., 2009; Sheldon et al., 2009a; von der Linden et al., 2014), where small distortions of an immense number of background objects are used to statistically determine the mass profile of a foreground halo.

Another common method of estimating the mass of groups and clusters is through the assumption of *hydrostatic equilibrium* (HSE). If the gas in clusters is in hydrostatic equilibrium with the cluster potential, then the pressure gradient offsets the

gravitational force:

$$\frac{dP(r)}{dr} = -\frac{G M(< r) \rho_{gas}(r)}{r^2} \quad (2.1)$$

Therefore, assuming the ICM is in hydrostatic equilibrium with the cluster potential, the total mass profile can be reconstructed from the observed gas density and pressure profiles:

$$M(< r) = -\frac{r^2}{G \rho_{gas}(r)} \frac{dP(< r)}{dr} . \quad (2.2)$$

Alternatively, the total mass can be obtained from the density and temperature profiles, assuming the ICM behaves as an ideal gas, $P(r) = n(r)kT(r)$:

$$M(< r) = -\frac{k T(r) r}{G} \left(\frac{d \log \rho_{gas}(r)}{dr} + \frac{d \log T(r)}{dr} \right) . \quad (2.3)$$

Gas density is typically measured using X-ray observations, as it is easily determined from the X-ray surface brightness. Temperature is determined from X-ray spectroscopy, and pressure is measured directly through the thermal SZ effect.

Whether the total mass obtained through the assumption of hydrostatic equilibrium (or the “hydrostatic mass”) is biased relative to the true mass is highly debated, as sources of non-thermal pressure (including cosmic rays, merger-induced shocks, and AGN feedback) can invalidate the assumption of hydrostatic equilibrium. Comparing hydrostatic masses to masses derived through weak lensing analysis can help constrain the bias inherent in the HSE assumption. In Section 4.1.1, we discuss observational and theoretical constraints on the hydrostatic mass bias.

The total matter density distribution is often modeled by the NFW profile, an analytic equation first proposed by Navarro et al. (1996) to describe the “universal density profile” of simulated dark matter halos, regardless of size. The NFW profile

has the form:

$$\rho_m(r) = \frac{\delta_c \rho_{crit}}{(r/r_s)(1 + r/r_s)^2} . \quad (2.4)$$

r_s is a characteristic radius representing the central core of the dark matter halo, ρ_{crit} is the critical matter density, and δ_c is a normalization constant which sets the characteristic overdensity of the cluster. Halos which fit the NFW profile are self-similar, in that r_s and δ_c are determined uniquely by the total halo mass. When $r \lesssim r_s$, the density profile decreases slowly ($\rho_m \propto r^{-1}$), while at $r \gg r_s$ the profile steepens significantly ($\rho_m \propto r^{-3}$). Observations of group and cluster halos consistently find that the total mass profile follows the NFW profile well (e.g., Vikhlinin et al., 2006; Mandelbaum et al., 2008; Sheldon et al., 2009a; Umetsu et al., 2009).

Several “mass proxies” have been used to estimate the total mass of groups and clusters. Mass proxies are typically easily-observed quantities that are found to correlate strongly with the total cluster mass. Examples include the X-ray temperature ($kT_X \approx 1 - 10$ keV for groups and clusters), the richness (number of bright galaxies observed within the cluster), the X-ray luminosity, and $Y_X = M_{gas}T_X$. Using mass proxies allows observers to place loose constraints on the mass of a cluster without requiring deep observations to recover the true gas or mass density profiles. The assumption of hydrostatic equilibrium can also affect the determination of mass through this method, as many Mass-Proxy relations are calibrated against hydrostatic masses of clusters (e.g., Arnaud et al., 2007, 2010).

2.2 Group and Cluster Gas Mass Fractions

The baryonic content of galaxy groups and clusters is dominated by hot plasma in the intracluster medium (ICM). Until very recently, the most sensitive X-ray and SZ observations were only able to constrain the gas mass in the ICM in the inner regions of groups and clusters, typically to around r_{500} (e.g., Vikhlinin et al., 2006; Arnaud

et al., 2007; Sun et al., 2009). Because r_{vir} is about twice r_{500} , these observations only probe the inner $\approx 1/8$ of the virial volume of groups and clusters. In order to measure the baryon distribution within the entire halo of groups and clusters, it is important to consider the gas within a volume substantially larger than that within r_{500} . Here, we describe the relevant observations of groups and clusters which measure both the ICM and total mass of the cluster. Because very few observations retain the sensitivity required to measure the gas density in the outskirts of clusters, we also discuss a method of using measured gas density profiles to extrapolate observed gas fractions to larger radii.

2.2.1 Observations

Vikhlinin et al. (2006) derived the gas and total mass profiles of 10 low-redshift (median redshift $z = 0.06$) relaxed clusters using long-exposure *Chandra* observations. The clusters have a median mass $M_{vir} = 7.3 \times 10^{14} M_{\odot}$, and range from $M_{vir} = 1.1 \times 10^{14} - 1.5 \times 10^{15} M_{\odot}$. Temperatures range from $kT = 2 - 9$ keV. The authors measured X-ray temperature and surface brightness profiles to approximately r_{500} . They modeled the surface brightness profile (which is proportional to $n_e n_p$) to recover the gas particle density, $\rho_{gas}(r)$. The total mass (M_{500}) was measured by solving the equation of hydrostatic equilibrium, using the observed density and temperature profiles, and is well-fit by an NFW profile in most cases. The integrated gas density and total mass profiles were used to derive the gas fraction interior to r_{500} , $f_{gas,500}$. This gas fraction ranges widely from cluster to cluster, from 6% to 14%, with median 11%. These observations were also used to derive a useful scaling relation between M_{500} and the X-ray temperature T :

$$M_{500} = (2.97 \pm 0.15) \times 10^{14} M_{\odot} h_{70}^{-1} \left(\frac{T}{5 \text{ keV}} \right)^{1.58 \pm 0.11}. \quad (2.5)$$

Arnaud et al. (2007) used very similar methods to derive the gas and total mass profiles of 10 low-redshift (median $z = 0.09$) relaxed clusters from *XMM-Newton* observations. The clusters range in mass from $M_{vir} = 1.2 \times 10^{14} - 1.16 \times 10^{15} M_{\odot}$, with a median of $4.2 \times 10^{14} M_{\odot}$, and temperatures vary from $kT = 2 - 8$ keV. The total mass also relies on the assumption of hydrostatic equilibrium, and was extrapolated from $\approx r_{700}$ to r_{500} using an NFW profile. f_{gas} was derived out to r_{500} for these clusters, varying from 5.5% to 16%, with median 11%, similar to the Vikhlinin et al. (2006) measurements.

Sun et al. (2009) analyzed the gas fraction in 43 groups from archival *Chandra* observations. All the groups are at low redshifts ($z \lesssim 0.1$). Of these 43 observations, 11 were sensitive enough to measure the X-ray surface brightness to r_{500} , while an additional 12 measured surface brightness to r_{1000} and were extrapolated to r_{500} . The total mass of the 23 best-measured groups ranges from $M_{vir} = 2.0 \times 10^{13} - 2.1 \times 10^{14} M_{\odot}$, with a median of $1.1 \times 10^{14} M_{\odot}$, and ICM temperatures range from $kT = 0.7 - 2.7$ keV. The total mass (assuming hydrostatic equilibrium) and gas mass were obtained using similar principles to Vikhlinin et al. (2006), with errors estimated by using 1000 artificial profiles generated from Monte-Carlo simulations. $f_{gas,500}$ for these 23 groups ranges from 5% – 11%, with a median of 8%, lower than for the more massive clusters of Vikhlinin et al. (2006) and Arnaud et al. (2007).

The above three samples were combined in the analysis of **Giodini et al. (2009)** (G09), which used all 10 clusters from Vikhlinin et al. (2006), all 10 clusters from Arnaud et al. (2007), and 21 of the 23 best-measured groups from Sun et al. (2009) to study the group/cluster gas mass fraction over a wide range of total masses. The authors binned the 41 groups and clusters logarithmically by mass, highlighting that lower mass groups have significantly lower gas fractions. The best-fit trend is:

$$f_{gas}(< r_{500}) = (9.3 \pm 0.2) \times 10^{-2} h_{70}^{-3/2} \left(\frac{M_{500}}{2 \times 10^{14} M_{\odot}} \right)^{0.21 \pm 0.03}. \quad (2.6)$$

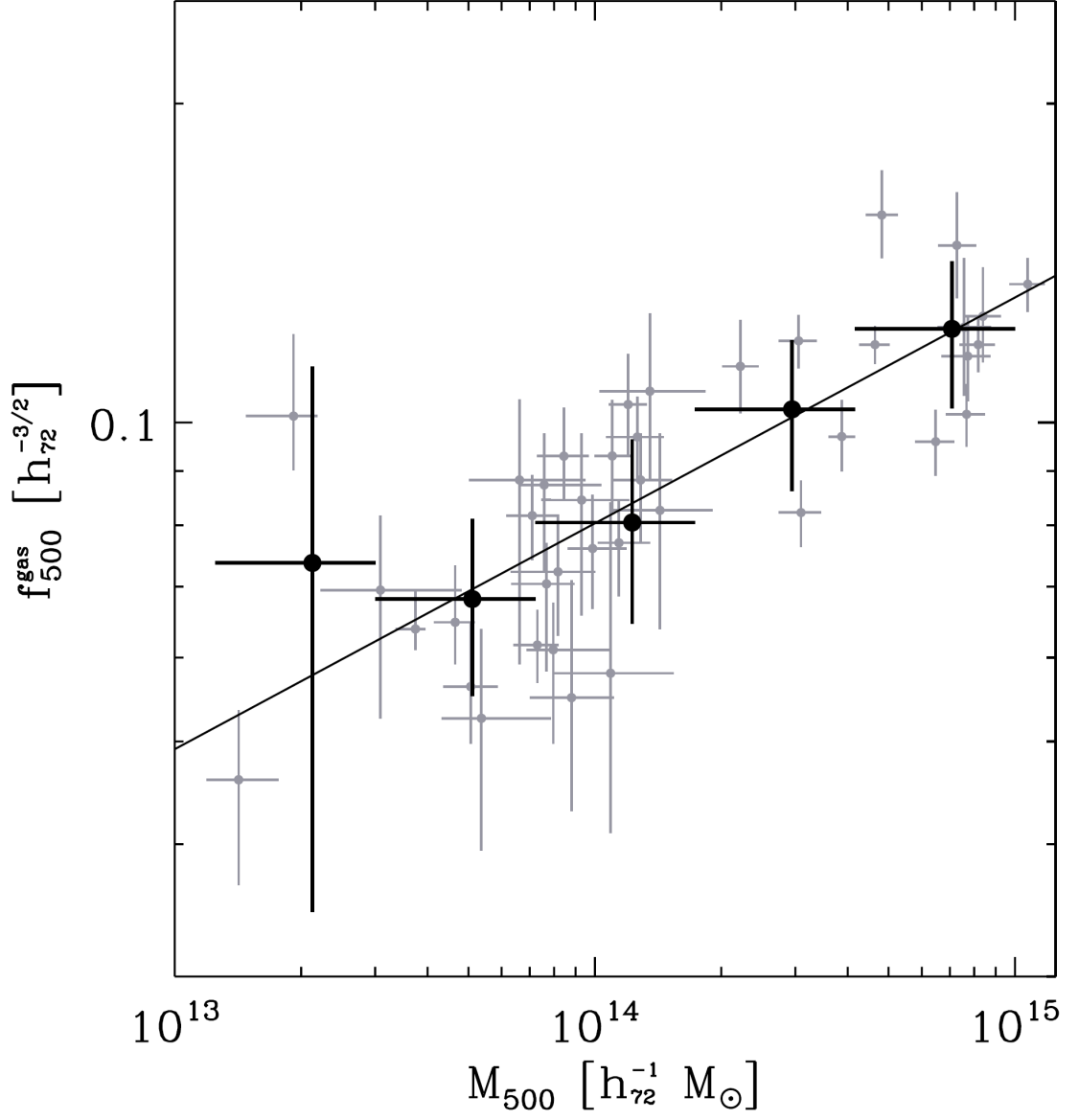


Figure 2.1: The dependence of $f_{gas}(< r_{500})$ on M_{500} ($\sim 0.73M_{vir}$), as presented in Giodini et al. (2009). The light-grey points represent individual group/cluster observations from Vikhlinin et al. (2006), Arnaud et al. (2007), and Sun et al. (2009), while the dark points are the average gas fractions, binned logarithmically with mass. Lower-mass halos show significantly lower gas fractions, with $f_{gas}(< r_{500})$ scaling roughly as $M_{500}^{0.21}$.

Figure 2.1 shows the distribution of the observed gas fractions, as a function of virial mass, measured by the three works above. We will use the G09 bins as 5 independent samples of f_{gas} for different masses.

Recent results from the *Planck* satellite detected the ICM using the thermal SZ effect, which measures the integrated line-of-sight gas pressure. **Planck Collaboration (2013d)** (hereafter PC13) derived a stacked pressure profile for 62 massive clusters that have archival observations with *XMM-Newton*. The cluster sample (detailed in Planck Collaboration, 2011) includes clusters of mass $M_{vir} = 3.3 \times 10^{14} - 2.7 \times 10^{15} M_{\odot}$, with median mass approximately $M_{vir} = 8.70 \times 10^{14} M_{\odot}$. X-ray temperatures range from $kT = 3.4 - 13$ keV. Total mass (M_{500}) was determined from a scaling relation with the quantity $Y_X = M_{gas}T_X$, an observable quantity that has been found to be a good mass proxy. The scaling relation in question (Arnaud et al., 2010) was calibrated against X-ray derived hydrostatic masses, and so the total mass of the stacked *Planck* clusters assumes hydrostatic equilibrium. The total mass beyond r_{500} was determined assuming an NFW profile. The stacked pressure profile is measured to unprecedented scales ($3r_{500} \approx 1.6r_{vir}$), although the X-ray temperature profile measured by *XMM-Newton* only extends to r_{500} , so the authors extrapolated the observed temperature profile to $3r_{500}$ to match the pressure observations.

Assuming the ICM acts as an ideal gas ($P = n_e kT$), the authors inverted the pressure and temperature profiles to retrieve the gas density profile and derive $f_{gas}(< r)$ out to $3r_{500}$ ¹. The reconstruction of the temperature profile was initially flawed, and the correct gas fraction profile was given in an erratum, Planck Collaboration (2013c). The gas fraction increases from r_{500} to r_{vir} (as indeed shown by Rasheed et al., 2011, see 2.2.2), reaching a peak of $\approx 15 \pm 2\%$ at $1.6r_{vir}$.

Eckert et al. (2013a) (E13) combined the stacked pressure profile from Planck Collaboration (2013d) with a stacked X-ray surface-brightness profile that directly

¹The authors also derive the gas fraction assuming a conservative case in which the ICM is isothermal beyond r_{500} , resulting in lower f_{gas} .

constrains the gas density to r_{200} . The X-ray observations were performed with *ROSAT*, on a sample of 31 clusters ($z \lesssim 0.2$) of temperatures $kT = 2.5 - 9$ keV, with median $kT = 6.5$ keV. The cluster masses range from $M_{vir} \approx 1.4 \times 10^{14}$ to $1.0 \times 10^{15} M_{\odot}$, with median $M_{vir} = 6.0 \times 10^{14} M_{\odot}$ ². The *Planck* pressure profile, combined with the gas density profile, was used to determine the total mass, assuming hydrostatic equilibrium. This is different from the method used by Planck Collaboration (2013d), which used a scaling relation and assumed an NFW profile. However, both estimates rely on the assumption of hydrostatic equilibrium either explicitly or implicitly through calibration of the $Y_X - M_{500}$ relation. 18 clusters are in common between the *ROSAT* and *Planck* samples, and the authors separated them into cool-core (CC, 6 clusters) and non-cool core (NCC, 12 clusters) categories. The gas fraction profile was determined separately for the two categories, and the authors found that NCC clusters have significantly higher gas fractions within r_{200} (0.169 ± 0.010) than relaxed, CC clusters do (0.134 ± 0.011), suggesting that the irregular, non-spherical morphologies of the disturbed clusters may bias the gas fractions high. They also found that f_{gas} increases from r_{500} to r_{200} ($f_{gas,500} \approx 0.12$ for CC clusters).

Umetsu et al. (2009) (U09) observed the ICM of four very massive ($M_{vir} \gtrsim 1 \times 10^{15} M_{\odot}$, $kT \approx 9 - 10$ keV) clusters using thermal SZ measurements with the *AMiBA* CMB telescope. After deriving pressure profiles from the SZ effect, the authors obtained the gas density profile using archival X-ray temperature measurements and a theoretically-derived temperature profile (Komatsu & Seljak, 2001). The authors use *Subaru* observations to derive the cluster masses with weak lensing analysis. The average gas fraction is determined to the limit of the SZ observations, r_{200} , and is observed to be $f_{gas}(< r_{500}) = 0.126 \pm 0.019$ within r_{500} and $f_{gas}(< r_{200}) = 0.133 \pm 0.020$ within r_{200} . These observations also find that f_{gas} increases with radius beyond r_{500} , in agreement with Rasheed et al. (2011), Planck Collaboration (2013d), and Eckert

²The authors do not give the masses of the clusters, so these values are taken from the $M - T$ relation of Vikhlinin et al. (2006) (our equation 2.5).

et al. (2013a). We emphasize that the total mass for these clusters is *not* dependent on the assumption of hydrostatic equilibrium (because they were derived using weak lensing measurements). See our discussion of the hydrostatic mass bias in Section 4.1.1.

Table 2.1 lists the observed data from the samples described above, including the most important characteristics of each sample: median mass (M_{vir}), whether that mass is derived assuming HSE, and the gas fraction at directly-observed radii.

Table 2.1: Samples of Groups/Clusters: Relevant Observations

Reference (1)	Clusters (2)	$\langle M_{vir} \rangle (M_{\odot})$ (3)	HSE? (4)	$f_{gas,500}$ (5)	$f_{gas,200}$ (6)	$f_{gas,vir}$ (7)
G09 Bin 1	2	2.9×10^{13}	✓	0.074 ± 0.028		
Bin 2	7	7.0×10^{13}	✓	0.068 ± 0.005		
Bin 3	17	1.7×10^{14}	✓	0.080 ± 0.003		
Bin 4	5	4.1×10^{14}	✓	0.103 ± 0.008		
Bin 5	10	9.8×10^{14}	✓	0.123 ± 0.007		
PC13	62	8.7×10^{14}	✓	0.125 ± 0.005	0.137 ± 0.003	0.145 ± 0.01
E13 - CC	6	5.9×10^{14}	✓	0.115 ± 0.010	0.134 ± 0.011	
U09	4	1.2×10^{15}	WL	0.126 ± 0.019	0.133 ± 0.020	

(1) G09, PC13, E13, and U09 stand for Giodini et al. (2009), Planck Collaboration (2013d), Eckert et al. (2013a), and Umetsu et al. (2009), respectively. CC represents the sub-sample of cool-core clusters.

(2) The number of clusters in each sample. (3) The median virial mass of the clusters.

(4) ✓ marks that the total mass assumes hydrostatic equilibrium. WL marks the mass was determined with weak lensing, and does not depend on the assumption of HSE.

(5) $f_{gas}(< r_{500})$ (6) $f_{gas}(< r_{200})$ (7) $f_{gas}(< r_{vir})$

2.2.2 Extrapolation of Gas Density Profiles

As seen above, very few observations retain the sensitivity necessary to measure the gas density to r_{vir} . Therefore, to constrain the gas fraction within the virial radius, we extrapolate the observed gas mass profile (at r_{200} or r_{500}) to larger radius by assuming a power-law profile:

$$\rho_{gas}(r) \propto r^{-\alpha_{gas}}, \quad (2.7)$$

where α_{gas} is the slope of the gas density profile, which can in general change as radius increases. The total matter density can be similarly modeled,

$$\rho_m(r) \propto (r)^{-\alpha_m}, \quad (2.8)$$

with α_m the slope of the total mass density profile. At large radii, the full equation for the gas fraction simplifies to approximately:

$$f_{gas}(< r) = \frac{M_{gas}}{M_{tot}} = \frac{\int_0^r 4\pi r'^2 \rho_{gas}(r') dr'}{\int_0^r 4\pi r'^2 \rho_m(r') dr'} \quad (2.9)$$

$$\propto \frac{\rho_{gas}(r)}{\rho_{tot}(r)} \quad (\text{at large } r)$$

$$\propto r^{\alpha_m - \alpha_{gas}}. \quad (2.10)$$

Therefore, the gas fraction can be extrapolated to larger radii using the difference in slopes between the gas density and total mass density profiles.

Rasheed et al. (2011) (R11) used this approach to extrapolate the gas fraction of the G09 cluster samples to r_{vir} . X-ray and SZ observations show that the gas density decreases more slowly with radius than the total mass density ($\alpha_{gas} < \alpha_m$), suggesting that the gas fraction increases when the cluster outskirts are considered. This is as expected if the gas is shock heated or supported by feedback pressure, and thus extends to larger radius.

R11 surveyed the literature to recover X-ray measurements which constrain the gas density slope nearly to r_{vir} . These measurements include observations with *ROSAT*, *Chandra*, *XMM-Newton*, and *Suzaku*, and cover a wide range of cluster masses and temperatures. Averaging over the many observations, the authors find that the observed gas density slope at r_{500} is steeper in with more massive clusters, with α_{gas} ranging from $\approx 1.8 \pm 0.2$ for poor clusters (G09 bin 2, $M_{vir} \approx 7 \times 10^{13} M_\odot$) to $\approx 2.3 \pm 0.02$ for the most massive G09 bin ($M_{vir} \approx 9.8 \times 10^{14} M_\odot$).

Compared to the gas density profile, the total density (NFW) profile is significantly steeper in the outer regions of the halo. The NFW profile has a slope of $\alpha_m = 2.6$ between r_{500} and r_{200} , and steepens to $\alpha_m = 2.7$ in the region r_{200} to r_{vir} . Therefore, R11 find that the gas fraction rises significantly beyond r_{500} . Because α_{gas} increases with cluster mass, the gas fraction rises more quickly with radius in groups and poor clusters ($f_{gas} \propto r^{0.8}$ for G09 bin 2) than in rich clusters ($f_{gas} \propto r^{0.3}$ for G09 bin 5). For these two bins, this yields an increase in f_{gas} by a factor of 1.6 and 1.2, respectively, from r_{500} to r_{vir} . This offers an explanation for the particular deficiency of baryons in low-mass clusters: the shallower gas profile implies the ICM is spread more broadly than in massive clusters, and the gas is extended further into the cluster outskirts.

We adopt R11's extrapolation model in order to approximate the gas fraction at r_{vir} in the samples which do not measure f_{gas} to these scales (all except PC13). α_{gas} for each sample in Table 2.1 is taken from the temperature-slope relation in R11; for consistency, we do not extrapolate the gas profiles for any individual cluster sample with coverage beyond r_{500} . We assume α_m as above for the NFW profile ($\alpha_m = 2.6$ for $r < r_{200}$, 2.7 for $r > r_{200}$). We extrapolate f_{gas} from the maximum observed radius, r_a , to a larger radius r_b using:

$$f_{gas,b} = f_{gas,a} \left(\frac{r_b}{r_a} \right)^{\alpha_m - \alpha_{gas}}. \quad (2.11)$$

For example, extrapolating the gas fraction of G09's bin 5 from r_{500} to r_{200} :

$$\begin{aligned} f_{gas,200} &= f_{gas,500} \left(\frac{r_{200}}{r_{500}} \right)^{\alpha_m - \alpha_{gas}} \\ &\approx 0.103 (1.45)^{2.6-2.3} \\ &\approx 0.115 \end{aligned} \quad (2.12)$$

To calculate the uncertainty on the extrapolated gas fraction, we propagate the

errors in $f_{gas,a}$ and in α_{gas} , making the simplification that no significant uncertainty exists in α_m or r_b/r_a . The fractional errors add in quadrature.

$$\frac{\Delta f_{gas,b}}{f_{gas,b}} = \sqrt{\left(\frac{\Delta f_{gas,a}}{f_{gas,a}}\right)^2 + \left(\frac{\Delta (r_b/r_a)^{\alpha_m - \alpha_{gas}}}{(r_b/r_a)^{\alpha_m - \alpha_{gas}}}\right)^2}. \quad (2.13)$$

The uncertainty in the right term is

$$\Delta (r_b/r_a)^{\alpha_m - \alpha_{gas}} = (r_b/r_a)^{\alpha_m - \alpha_{gas}} \ln(r_b/r_a) \Delta \alpha_{gas}, \quad (2.14)$$

yielding the final result:

$$\frac{\Delta f_{gas,b}}{f_{gas,b}} = \sqrt{\left(\frac{\Delta f_{gas,a}}{f_{gas,a}}\right)^2 + (\ln(r_b/r_a) \Delta \alpha_{gas})^2}. \quad (2.15)$$

The gas density profile is expected to steepen at very large radii, such that it eventually matches the NFW profile (e.g., Umetsu et al., 2009), which translates to the gas fraction asymptotically approaching a constant value. At large enough radius, extrapolation of the gas fraction as described above will, therefore, become invalid, as α_{gas} will not remain fixed. The range at which the gas density steepens significantly is not known, however, as observational data does not currently constrain α_{gas} far beyond r_{200} . We assume α_{gas} remains constant to r_{vir} (and slightly beyond), and emphasize that the our estimate of the gas fraction will be biased high if the gas density slope steepens significantly beyond r_{200} . In Section 4.1.3, we discuss current constraints on this steepening of this slope.

2.3 Group and Cluster Stellar Mass Fractions

The integrated stellar mass of groups and clusters is also an important (although subdominant) reservoir of baryons in these large systems. The stellar mass of clusters

is thought to come almost entirely from the stellar content of the individual cluster galaxies (plus an estimated $\approx 10\%$ from the diffuse intracluster light).

G09 estimated the stellar content of a large number (> 90) of groups and clusters from the *COSMOS* survey. Using optical and infrared observations from *Subaru*, the authors fit a broad-band spectrum to the detected galaxies in each cluster and used their spectral energy distributions to derive photometric redshifts for the sample. Converting the *Ks*-band (IR) luminosity of detected galaxies to stellar mass, and accounting for the entire predicted galactic mass function, G09 determined the stellar fraction in clusters of masses $1 \times 10^{13} - 1 \times 10^{15} M_{\odot}$. At r_{500} , the stellar fraction was found to be significantly higher ($\approx 6\%$) for groups and poor clusters than for the most massive clusters ($\approx 2\%$). The authors derived a fit to stellar-fraction versus mass of:

$$f_*(< r_{500}) = (5.0 \pm 0.1) \times 10^{-2} \left(\frac{M_{500}}{5 \times 10^{13} M_{\odot}} \right)^{-0.37 \pm 0.04}. \quad (2.16)$$

The results of an extensive Sloan Digital Sky Survey (SDSS) weak lensing study of stacked groups and clusters has placed unparalleled constraints on the stellar fraction in groups and clusters. The MaxBCG sample (Sheldon et al., 2009a) contains $> 130,000$ groups and clusters between redshifts $z = 0.1 - 0.3$. Sheldon et al. (2009b) binned the clusters by richness and luminosity, and stacked by centering on the brightest cluster galaxy (BCG). The mean weak lensing profile was observed well into the surrounding large scale structure ($\gtrsim 15 - 20 r_{vir}$), as was the averaged optical surface brightness, allowing the total mass to light ratio (M/L) to be obtained. **Bahcall & Kulier (2014)** (BK14) determined the observed mass-to-light distribution as a function of environment and scale. They combined this with the observed stellar mass to light ratio of individual spiral and elliptical galaxies and their relative abundance from the density-morphology relation, and used it to determine the stellar mass fraction as a function of radius and for groups and clusters of various masses.

Figure 2.2 shows the cumulative and local stellar fraction distributions derived by

BK14. The stellar fraction is determined at r_{200b} ³ as a function of cluster mass. The authors find that the stellar fraction at this fixed radius decreases with virial mass, in good agreement with G09. The stellar fraction is also obtained as a function of radius, divided into three richness bins, with mass ranges corresponding approximately to $M_{vir} < 2 \times 10^{13} M_{\odot}$, $2 \times 10^{13} M_{\odot} < M_{vir} < 1 \times 10^{14} M_{\odot}$, and $M_{vir} > 1 \times 10^{14} M_{\odot}$. The cumulative stellar fraction decreases significantly from the centers of groups and clusters, asymptotically approaching at high radius a “cosmic stellar fraction” of $f_{*} \approx 0.01 \pm 0.004$ in all richness bins. The local stellar fraction is approximately the cosmic fraction at all scales above roughly 300 kpc, the scale of the BCG. The higher cumulative stellar fraction at any radius in groups and poor clusters suggests that their stellar masses are more dominated by the BCG than massive clusters.

2.4 Galaxy Mass Fractions

Studying the distribution of baryons in individual galaxies presents many other challenges not faced in the investigation of clusters. Because galaxy systems are significantly lower mass than clusters ($M_{vir} \approx 1 - 2 \times 10^{12} M_{\odot}$ for a typical L^{*} galaxy), their gravitational wells are shallower, and it is easier for feedback effects to remove gas from the systems altogether (e.g., Oppenheimer et al., 2010). The lower total mass also translates to a much lower thermal temperature for the gas to be in hydrostatic equilibrium. Therefore, the main diffuse gaseous component of galactic system will primarily be too cool and low density to be detected in emission.

The most obvious and easily detected baryon reservoir in (L^{*}) galaxies is the galactic disk itself, which contains the stellar population as well as the gas and dust of the ISM. Baryons are also stored in the “circumgalactic medium” (CGM), a large, diffuse region surrounding galaxies with low temperatures and densities. Observations

³ r_{200b} represents where the density is 200 times the cosmic matter density, not the critical density, and corresponds roughly to our definition of r_{vir} .

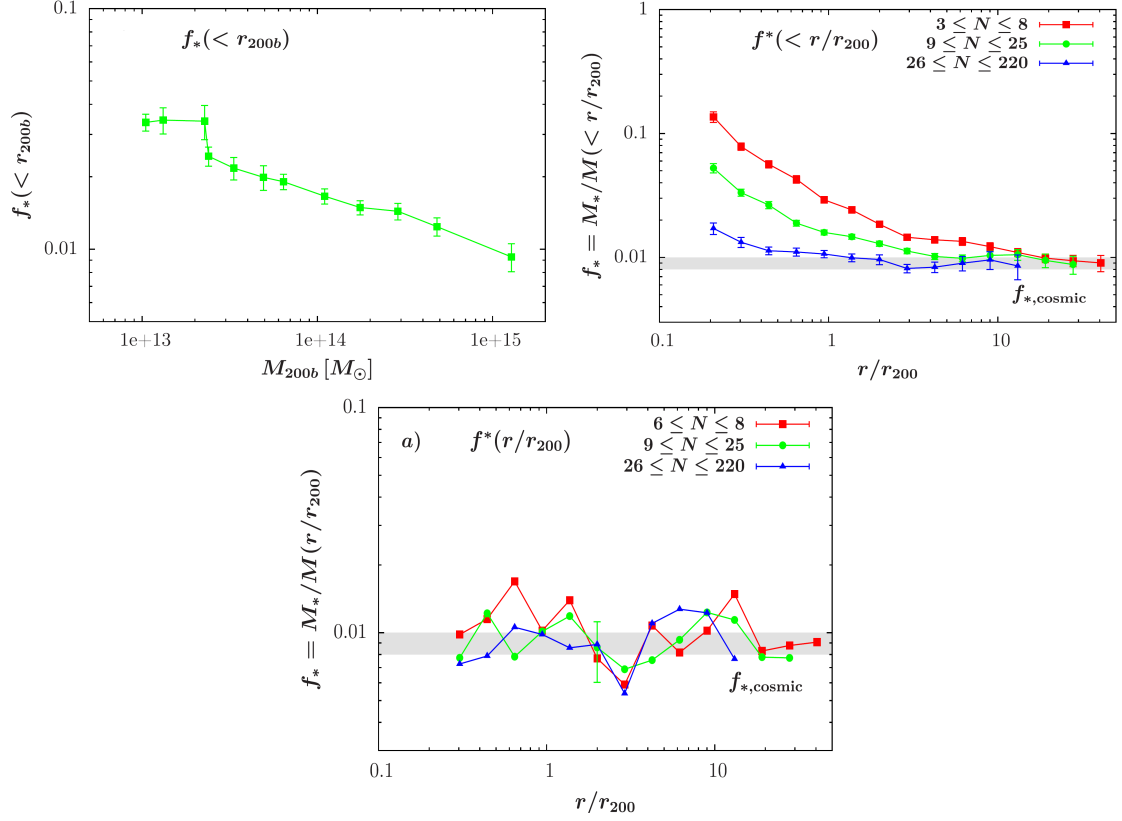


Figure 2.2: The stellar fraction from stacked optical and weak lensing observations, as presented in Bahcall & Kulier (2014). *Upper left*: The cumulative stellar fraction within $r_{200b} \approx r_{vir}$ in groups and clusters, as a function of total mass. f_* decreases in more massive clusters, in agreement with observations collected by Giodini et al. (2009). *Upper right*: The cumulative stellar fraction as a function of halo-centric radius. The profiles are binned by richness, a proxy for mass. More massive clusters have lower stellar fraction at any given radius (lower mass halos are more dominated by their BCGs), but the stellar fraction tends towards a constant value at high radius irrespective of mass: the “cosmic stellar fraction” $\approx 1\%$. *Lower*: The local stellar fraction of all groups and clusters, regardless of richness, is approximately 1% at all scales above the BCG.

are beginning, for the first time, to place reasonable constraints on the total mass in this baryonic phase, allowing estimates of the makeup, distribution, and total fraction of baryons in the low-mass halos of galaxies.

2.4.1 The Circumgalactic Medium

The existence of the CGM was first predicted by Bahcall & Spitzer (1969) to explain the presence of absorption features in the spectra of quasars. The emission from quasars was known to come from high redshift, while the absorption lines came from lower redshifts (typically $z = 1 - 3$), had low dispersion velocities, and showed the presence of many abundant elements and ionization states (including absorption from H I, C II, C IV, Si II, and many others). The authors predicted that an extended halo of gas ($r \approx 10^2$ kpc) surrounding normal galaxies ($M \approx 10^{11} - 10^{12} M_{\odot}$) could produce the observed absorption profiles and dispersion velocities. Even at this early stage, many separate phases of the CGM were predicted, as temperatures ranging from $2 \times 10^4 - 2 \times 10^5$ K were required to explain the variety of ionization states.

Very recently, observations have confirmed this hypothesis by associating the absorption features in QSO sightlines to nearby foreground galaxies with the expected redshifts. The CGM is a gaseous reservoir in the dark matter halo around galaxies, which extends for several hundred kiloparsecs, and likely as far as the virial radius ($r_{vir} \approx 300$ kpc for an L^* galaxy). The CGM is also likely the major source of pristine gas accreting onto the galactic disk.

The use of QSO and galaxy absorption spectroscopy remains the most powerful tool in statistically characterizing the CGM. The high spatial density of background galaxies and quasars results in a large number of sightlines through the CGM at a wide variety of projected distances. While it is very unlikely to have enough bright background sources to resolve the distribution of the CGM in any individual galaxy, it is possible to recover the average profile of gas absorption in many galaxies as a

function of radius by stacking many sightlines together by the projected distance from their absorbing galaxy.

Steidel et al. (2010) used a sample of 512 galaxy pairs, where both foreground and background galaxies have spectroscopic redshifts and are separated by less than 15'' on the sky. At the median redshift of the foreground absorbers ($z \approx 2$), this translates to projected distances within 125 kpc. Absorption profiles (stacked into three projected radius bins) were measured for Ly α , C IV (1549Å), C II (1334Å), Si IV (1393Å), and Si II (1260Å and 1526Å). Hydrogen, the most dominant element by mass in the CGM, is measured in its neutral phase through Ly α absorption, and is observed well beyond 100 kpc. Using an approximate model for populating the CGM by galactic outflows, the authors placed a rough constraint on the CGM mass of $M_{CGM} \approx 3 \times 10^{10} M_{\odot}$, although we emphasize that this is only an order-of-magnitude estimate. By this approximation, the CGM contains roughly the same mass as the sum of stars and gas in the stellar disk, and amounts to $\approx 3 - 4\%$ of the total mass of the dark matter halo ($\approx 20\%$ of the expected baryonic mass, assuming the halo contains the entire cosmic baryon fraction).

The COS-Halos survey (Tumlinson et al., 2011) was designed specifically to study the CGM in low-redshift galaxies. It uses far-UV spectroscopy of background quasars behind 44 roughly L^* galaxies, observed with the Cosmic Origins Spectrograph instrument on the Hubble Space Telescope. Measuring the column density in Ly α , early results (Thom et al., 2012; Werk et al., 2013) placed a very conservative lower limit on the CGM gas mass of $M_{CGM} > 10^9 M_{\odot}$. Later analysis by **Werk et al. (2014)** (W14) developed a model for the ionization state of the CGM, constrained by the observed absorption of low, intermediate, and high-ionization transitions in metals. This model – which indicates that the hydrogen in the CGM is increasingly ionized at larger radii – was used to greatly improve the limits on the CGM mass. Integrating the best-fit gas density profile to the virial radius (300 kpc), they

found that the cool phase ($T \approx 10^4 - 10^5$ K) of the CGM in L^* galaxies has a mass of $M_{CGM} \approx 7 \times 10^{10} - 1.2 \times 10^{11} M_\odot$. This CGM mass is larger than, although consistent with, the rough estimate made by Steidel et al. (2010), and is similar to the combined mass of the stellar disk and ISM. The uncertainty in M_{CGM} is dominated by saturation in a few Ly α absorption profiles. The minimum CGM mass is $M_{CGM} > 6.5 \times 10^{10} M_\odot$, and could range as high as $M_{CGM} \approx 1.2 \times 10^{11} M_\odot$ if all saturated column densities are 3 times higher than their lower limits. The total virial mass of L^* galaxies is approximately $1.6 \times 10^{12} M_\odot$, so the authors conclude the cool CGM accounts for 25 – 45% of the expected baryonic mass in galaxies ($M_b = f_{b,cosmic} M_{vir} \approx 2.6 \times 10^{11} M_\odot$).

2.4.2 Estimate of The Galactic Baryon Fraction

W14 combined their estimate of the cool gas mass in the CGM with observations of other baryonic components of galactic systems to constrain the total baryon fraction currently detected within the virial radius. The median stellar mass of the COS-Halos galaxies is $\langle M_* \rangle = 4 \times 10^{10} M_\odot$, in agreement with abundance matching estimates (Behroozi et al., 2010). The gaseous component of the ISM, observed with HI surveys, can vary from very little (for elliptical galaxies) to of order the stellar mass (McGaugh et al., 2010; Martin et al., 2010). Together, for a star-forming L^* galaxy, the mass of the stellar and gaseous disk (the normal galactic component) is given as $7 \times 10^{10} M_\odot$. Thus, the disk contributes about 4 – 5% of the total mass of the galactic system, or about 27% of the expected baryon content.

The presence of high-ionization absorption lines in CGM profiles suggests that a warm ($> 10^5$ K) CGM component exists. The ionization model derived by W14 to fit the low-ionization transition abundances severely underestimates the column density of O VI. The authors reference models which predict a mass of warm CGM of at least $M_{CGM,warm} \gtrsim 10^{10} M_\odot$ to explain the observed O VI absorption (Peeples et al., 2014).

This mass estimate is highly sensitive to the assumed metallicity in the warm CGM phase, and decreasing Z from Z_{\odot} to $0.1Z_{\odot}$ increases the predicted warm CGM mass by a factor of 10. The constraints on the warm CGM fraction thus range from 0.6% to 6% of the total virial mass, or 4 – 40% of the expected baryon fraction.

X-ray observations hint at the existence of a hot ($> 10^6$ K) gaseous reservoir outside large galaxies. Estimates of the total mass of this X-ray component range from $10^9 - 10^{11} M_{\odot}$. W14 argues that, by extrapolating the observed mass of $\approx 10^9 M_{\odot}$, observed within 50 kpc of an L^* galaxy by *ROSAT* (Anderson et al., 2013), to 300 kpc could increase the mass by a factor of 6 – 14, although the density profile of this X-ray component is unconstrained. W14 adopts the range of $10^9 - 1.4 \times 10^{10} M_{\odot}$ for the X-ray CGM from this work. This is between $\approx 1\%$ to 5% of the expected baryonic mass, or $< 1\%$ of the total mass budget. Gupta et al. (2012), however, claims that the Milky Way may have a hot, X-ray reservoir with mass as high as $10^{11} M_{\odot}$, based on O VII and O VIII absorption observed with *XMM-Newton* and emission from the soft X-ray background. If this is true, the X-ray component of the CGM may be substantially larger than observed by Anderson et al. (2013).

Allow us to summarize the distribution of the expected baryonic mass ($M_b \approx 2.6 \times 10^{11} M_{\odot}$) in galactic halos, as described above and by Werk et al. (2014). The gas in the cool CGM has at least 25% and as much as 50% of M_b . The stellar disk contains $\approx 25\%$, depending on the amount of gas in the ISM. The warm CGM contains between 4% and 40%, and the X-ray CGM is thought to hold 1% – 5%. W14 concludes that current observations could be detecting the entire baryon fraction in galactic clusters, with the primary uncertainty resting on the contents of the warm CGM.

To fit a best estimate to the baryon fraction, we take the mean of the lower and upper limits on each component’s abundance, with the exception of the stellar-disk component, which we take to be the upper limit of 4.5% of the total virial mass from

stars and ISM. We take one-half the range on the limits as the uncertainty:

$$f_{disk}(< r_{vir}) = 0.045 \pm 0.013$$

$$f_{CGM,cool}(< r_{vir}) = 0.060 \pm 0.013$$

$$f_{CGM,warm}(< r_{vir}) = 0.035 \pm 0.025$$

$$f_{X-ray}(< r_{vir}) = 0.005 \pm 0.004$$

Summing these components and propagating uncertainties, assuming they are independent, yields our best estimate of the baryon fraction in galactic systems:

$$\mathbf{f_b}(< r_{vir}) = \mathbf{0.145 \pm 0.030} . \quad (2.17)$$

If the errors are not independent (and add linearly, not in quadrature), the true lower and upper limits on the baryon fraction in galactic systems are 9.5% and 19%, respectively.

Chapter 3

Results

3.1 The Distribution of Gas, Stars, and Baryons in Groups and Clusters

From the observations presented in Chapter 2, we have measurements of the gaseous component of the ICM in halos spanning the entire mass range from poor groups to the most massive clusters. We also have measurements of the stellar fraction well beyond the virial radius, gathered from stacked optical and weak lensing observations. Here, we show our results from this data and its analysis.

In Figure 3.1, we present the gas fraction in these groups and clusters as a function of radius, out to $1.2r_{vir}$. We use the extrapolation methods described in Section 2.2.2 when necessary for observations which only constrain the gas fraction within r_{500} or r_{200} . The gas fractions of each sample (both observed and extrapolated) are listed in Table 3.1. We discuss the potential biases in using the hydrostatic mass and extrapolating the gas density profile to $1.2r_{vir}$ in Section 4.1.

The gas fraction increases with radius in all groups and clusters. Comparing to the “expected” gas fraction of $\approx 15.4\%$, which is the difference between the WMAP9 cosmic baryon fraction (16.4%) and the cosmic stellar fraction of BK14 (1%), nearly

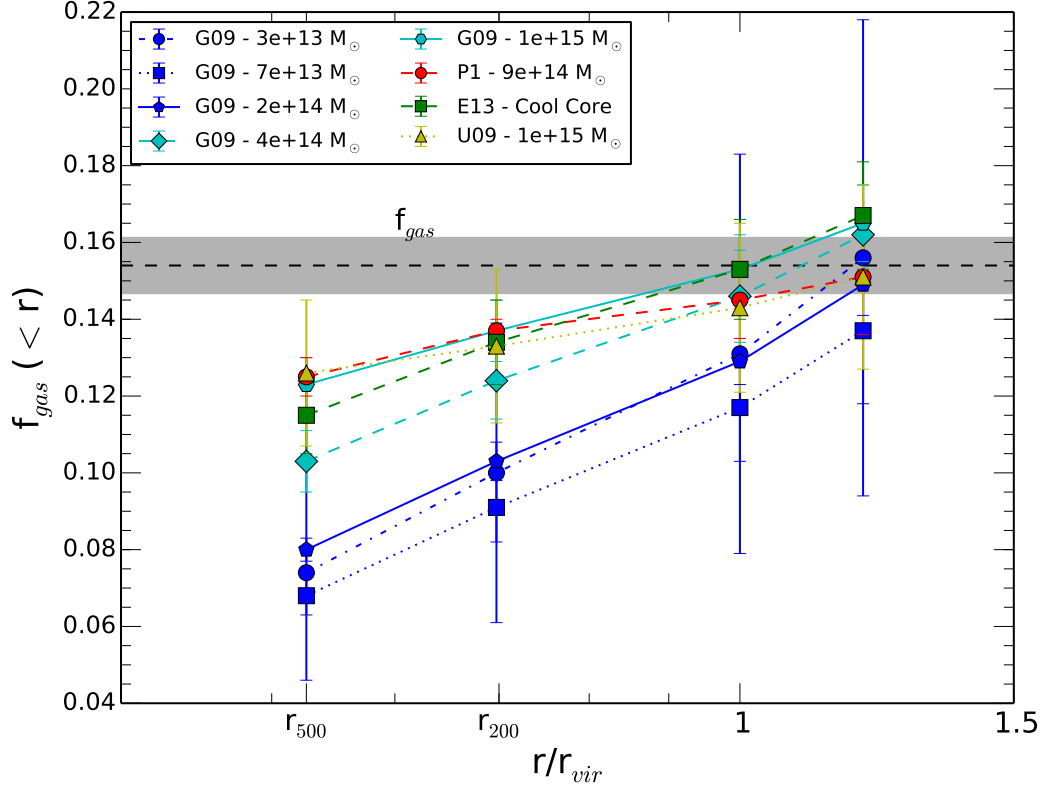


Figure 3.1: The cumulative hot gas fraction for each cluster sample in our study, plotted against the cluster-centric radius. Blue and cyan points (G09) represent data from Giodini et al. (2009), red points (P1) are temperature hypothesis 1 from Planck Collaboration (2013c), green points (E13) from Eckert et al. (2013c), and yellow points (U09) from Umetsu et al. (2009). See Section 2.2.1 for details of these sources. Many observations are extrapolated to $1.2r_{vir}$, as in Rasheed et al. (2011). The f_{gas} line represents the difference between the WMAP9 cosmic baryon fraction and the cosmic stellar fraction from Bahcall & Kulier (2014). We discuss possible biases in using the HSE mass and extrapolating the gas density profile in Section 4.1.

all clusters appear to contain the expected fraction of gas within the virial radius or $1.2r_{vir}$. A portion of the ICM is, therefore, “hidden” in the outskirts of groups and clusters, where earlier observations interior to r_{500} were not able to probe.

Table 3.1: Gas Fraction in Groups/Clusters: Observed and Extrapolated

Reference (1)	$\langle kT \rangle$ (2)	α_{gas} (3)	$f_{gas,500}$ (4)	$f_{gas,200}$ (5)	$f_{gas,vir}$ (6)	$f_{gas,1.2vir}$ (7)
G09 Bin 1	0.9 keV	1.7 ± 0.20	0.074 ± 0.028	$0.100 \pm 0.039^*$	$0.131 \pm 0.052^*$	$0.156 \pm 0.062^*$
Bin 2	1.6 keV	1.8 ± 0.20	0.068 ± 0.005	$0.091 \pm 0.009^*$	$0.117 \pm 0.014^*$	$0.137 \pm 0.019^*$
Bin 3	2.8 keV	1.9 ± 0.07	0.080 ± 0.003	$0.103 \pm 0.005^*$	$0.129 \pm 0.006^*$	$0.149 \pm 0.008^*$
Bin 4	5.0 keV	2.1 ± 0.02	0.103 ± 0.008	$0.124 \pm 0.010^*$	$0.146 \pm 0.012^*$	$0.162 \pm 0.013^*$
Bin 5	8.6 keV	2.3 ± 0.02	0.123 ± 0.007	$0.137 \pm 0.008^*$	$0.153 \pm 0.009^*$	$0.165 \pm 0.010^*$
PC13	†	†	0.125 ± 0.005	0.137 ± 0.003	0.145 ± 0.010	0.151 ± 0.009
E13 - CC	6.3 keV	2.2 ± 0.05	0.115 ± 0.010	0.134 ± 0.011	$0.153 \pm 0.013^*$	$0.167 \pm 0.014^*$
U09	9.7 keV	2.4 ± 0.10	0.126 ± 0.019	0.133 ± 0.020	$0.143 \pm 0.022^*$	$0.151 \pm 0.024^*$

(1) Reference abbreviations as in Table 2.1.

(2) The median temperature of the groups/clusters in each sample.

(3) The gas density slope derived from R11.

(4) $f_{gas}(< r_{500})$ (5) $f_{gas}(< r_{200})$ (6) $f_{gas}(< r_{vir})$ (7) $f_{gas}(< 1.2r_{vir})$

*: Value represents extrapolation using the method of Section 2.2.2.

†: No extrapolation required; T and α_{gas} not calculated.

Figure 3.2 shows the group and cluster gas fraction as a function of the virial mass of the system. The shortage of gas in low-mass clusters is apparent at r_{500} , with low-mass groups and clusters falling further short of the expected fraction than larger clusters. However, the shallower slope of the gas density profile in low-mass systems leads to a dramatic increase in the gas fraction when extrapolated to larger radius: from r_{500} to r_{vir} , their gas fraction has almost doubled. The gas distribution in low mass clusters is more extended, likely due to the shallow gravitational potential well. All systems from groups to massive clusters are consistent with containing the expected gas fraction interior to $\approx 1.2r_{vir}$. Gas is less centrally concentrated than dark matter, with a large fraction residing in the outskirts of groups and clusters, but within $1.2r_{vir}$ the gas mass traces the total mass well.

The mass of dark matter halos clearly has an important effect on the distribution of baryons, as the virial mass appears to determine how extended the baryonic dis-

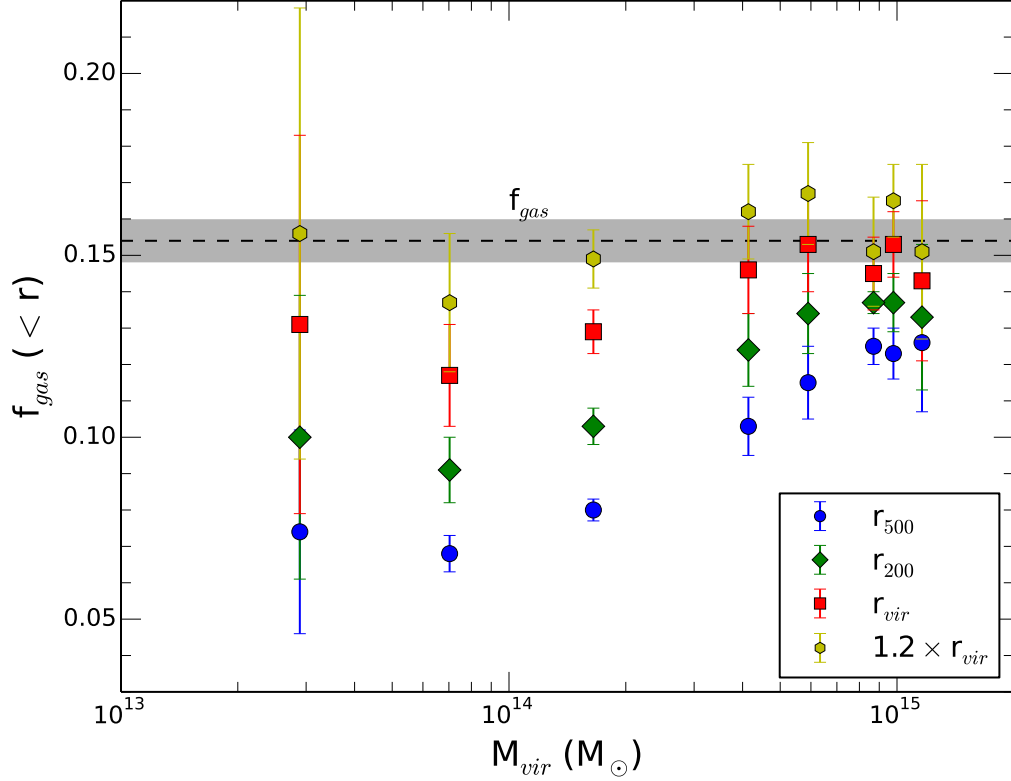


Figure 3.2: The cumulative hot gas fraction for each cluster sample in our study, plotted against the mean halo mass. Blue circles, green diamonds, red squares, and yellow hexagons show the gas fraction measured at r_{500} , r_{200} , r_{vir} , and $1.2r_{vir}$, respectively. The f_{gas} line represents roughly the expected hot-gas fraction, and is the difference between the *WMAP9* cosmic baryon fraction and the cosmic stellar fraction ($\sim 1\%$, Bahcall & Kulier, 2014).

tribution is. We therefore combine our samples of groups and clusters into two bins: groups/poor clusters ($M_{vir} < 3 \times 10^{14} M_{\odot}$), and rich clusters ($M_{vir} > 3 \times 10^{14} M_{\odot}$). In Figure 3.3, we show the averaged gas fraction in each bin, as a function of radius. Each point represents the weighted mean of gas fraction at that radius, for all clusters in that mass range. These mass bins translate roughly to the medium-richness and high-richness bins of BK14, respectively. Therefore, we also include the average stellar fraction, which is measured far beyond r_{vir} .

At r_{500} , the average gas fraction is $\approx 7.5\%$ in groups and poor clusters and $\approx 12\%$ in rich clusters. The gas fraction increases steeply in groups and poor clusters,

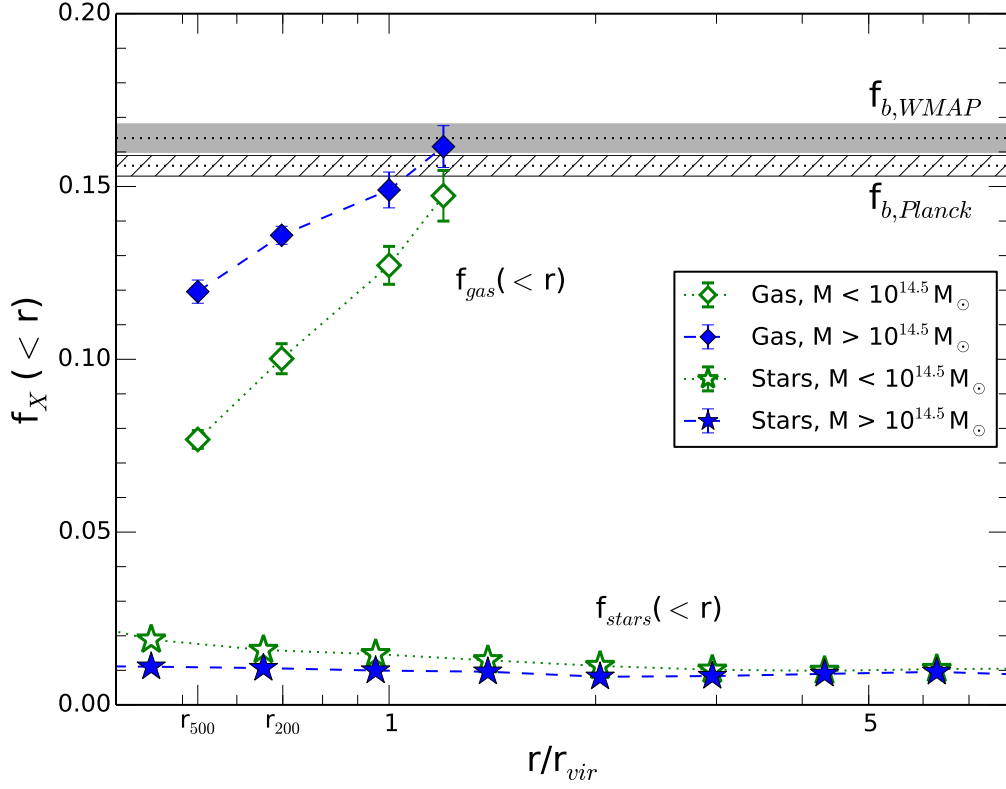


Figure 3.3: The cumulative stellar (Figure 2.2) and hot gas (Figure 3.1) fractions for groups and clusters, as a function of cluster-centric radius. Bahcall & Kulier (2014) presented the stellar fraction for various cluster richness bins. The gas fractions of Figure 3.1 have been sorted into corresponding bins, using the mass-richness relation of Sheldon et al. (2009b). The stellar fraction asymptotes to a “cosmic” stellar fraction at a few times r_{vir} , and the gas fraction increases and converges at high radius as well.

reaching about 13% at r_{vir} and 15% at $1.2r_{vir}$. In rich clusters, the gas fraction increases more slowly, reaching 15% at r_{vir} , and 16% at $1.2r_{vir}$, representing the increased concentration of gas in high mass clusters. The stellar fraction decreases from 2% at r_{500} to 1.5% at $1.2r_{vir}$ in the low-mass bin, and remains steady at 1% in the high-mass bin. We note that the apparent steepening of the f_{gas} profile at r_{vir} is simply a relic of the logarithmic scale of the X axis. As a whole, low mass clusters have lower gas fractions and higher stellar fractions at any given radius, with both distributions being more extended than in massive clusters.

We are now able to combine the gas fraction and stellar fraction for clusters in

these two mass ranges, yielding the total baryon fraction distribution. This is presented in Figure 3.4. The overall baryon fraction increases with radius, reaching the cosmic baryon fraction at $\approx r_{vir}$ in massive clusters and at $\approx 1.2r_{vir}$ in groups and poor clusters. The entire baryonic mass associated with the virial mass of groups and clusters is detected or inferred within the dark matter halo, indicating that the baryonic matter content of the universe is a strong proxy for the dark matter distribution, when averaged on appreciably large scales.

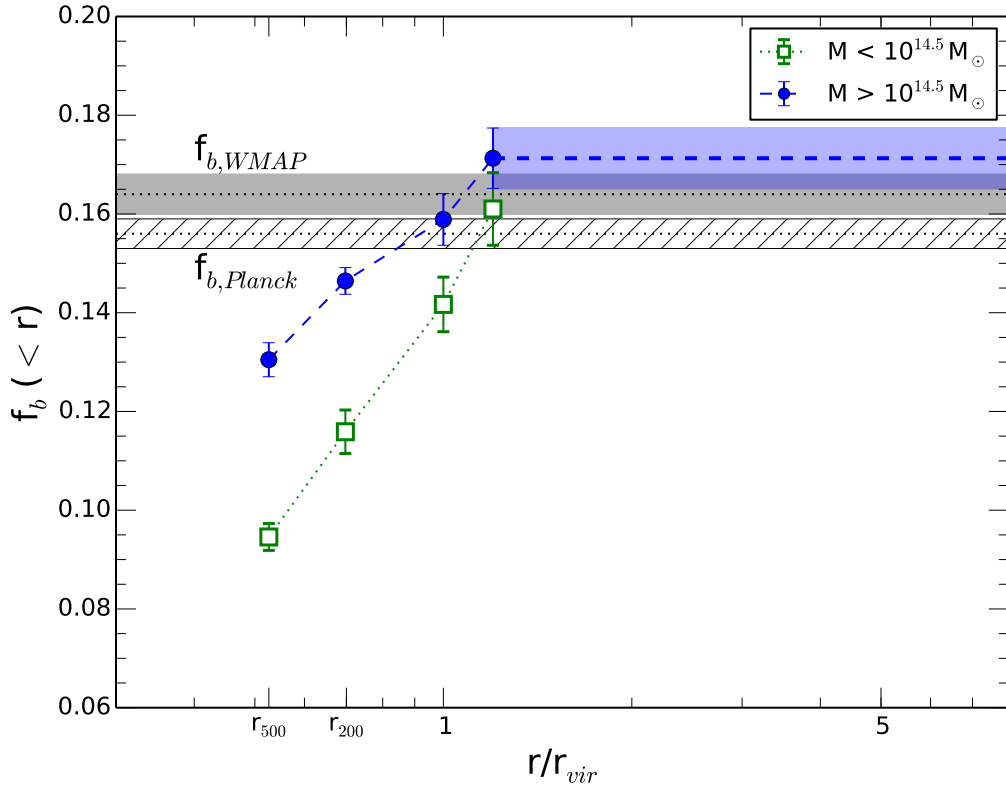


Figure 3.4: The cumulative baryon fraction for groups and clusters, as a function of cluster-centric radius. The baryon fraction (f_b) is the sum of the cumulative stellar fraction and the cumulative hot gas fraction of Figure 3.3. Green squares represent the averaged fractions of groups and smaller clusters, while blue circles represent larger clusters. The baryon fraction in large clusters appears to approach the cosmic fraction at large scales, and we extrapolate the value at larger scales as the value at $1.2r_{vir}$, an assumption we discuss in Section 4.1.3.

The stellar fraction is observed to approach a constant value at high radii (Bahcall

& Kulier, 2014). The gas fraction is predicted to do the same, as the gas density profile likely approaches the total mass (NFW) profile at high radius (e.g., Umetsu et al., 2009, and refs. therein). We approximate this by assuming that, beyond $\approx 1.2r_{vir}$, the gas fraction reaches a constant value, and represent this as an extrapolation of the baryon fraction out to high radius into the large-scale structure (LSS) in Figure 3.4. Therefore, current observations are consistent with the picture that the baryon distribution matches the distribution of matter well at all scales larger than the virial radius of clusters, and implies that the cosmic baryon fraction also populates the large-scale structure outside the virial radius of groups and clusters. The extrapolation to $1.2r_{vir}$ and not beyond is arbitrary, as the gas density slope likely steepens before this point. We discuss this simplification and the validity of our approximation in Section 4.1.3.

3.2 The Baryonic Content of Systems from Galaxies to Groups and Clusters

We have just shown that, within roughly the virial radius, dark matter halos of both group and cluster sizes are observed to hold the entire cosmic baryon fraction. Combined with the measurements of the baryonic components in galactic systems (Section 2.4.2), we are able to place global constraints on the baryon distribution within halos ranging over three orders of magnitude in mass.

Figure 3.5 presents the collection of observations on the baryon fraction in halos of a wide range of masses. Shown, as a function of mass, are the current limits on the baryon fraction for the previously mentioned samples of galaxies, groups, and clusters. Observations of the outskirts of groups and clusters show that the baryon fraction reaches the cosmic value between r_{vir} and $1.2r_{vir}$. We plot the group and cluster baryon fraction, which is the sum of the gas fraction (Figure 3.2) and stellar

fraction (Figure 2.2), at these two radii and sorted by mass. Observations of galactic systems show that – between the stellar disk and ISM, cold CGM, warm CGM, and X-ray CGM – the entire baryon fraction could be contained within the virial volume of galactic halos. We plot the baryon fraction range constrained by Werk et al. (2014), which includes lower and upper limits of $f_b(< r_{vir}) = 9\% - 19\%$. The best-estimate value, taking the mean of the ranges given for each component, is $14.5\% \pm 3\%$.

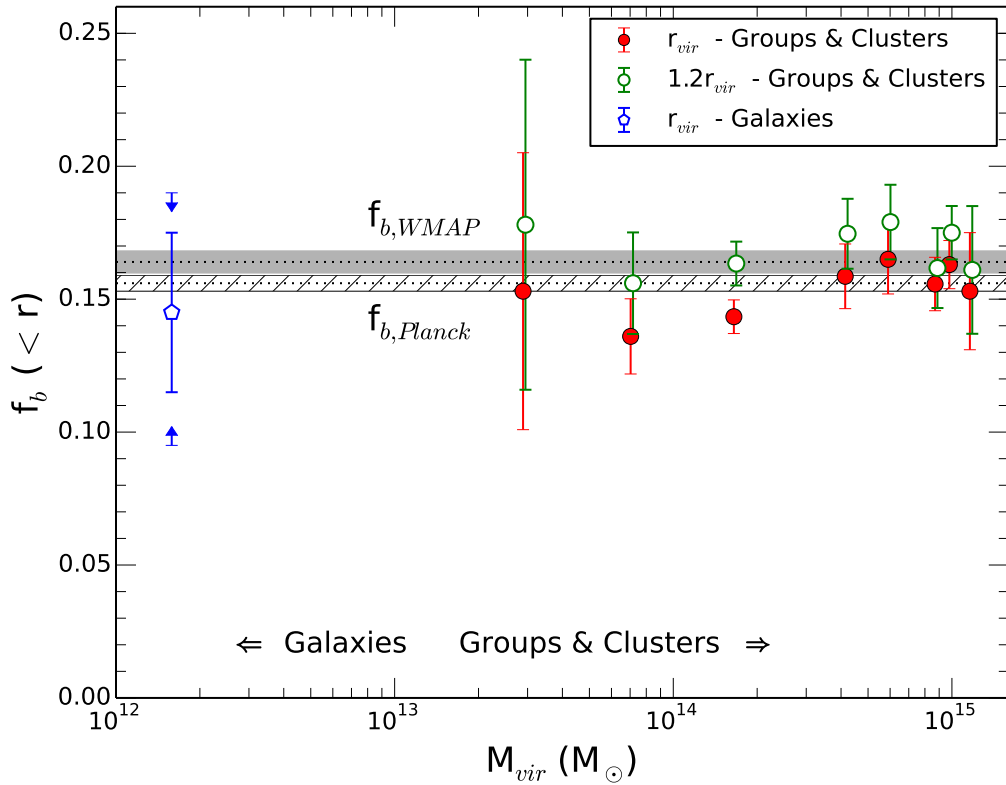


Figure 3.5: The cumulative baryon fraction (f_b) for galaxies, groups, and clusters, as a function of the average mass of the sample. The baryon fraction of groups and clusters (filled red points: within r_{vir} ; open green points: within $1.2r_{vir}$) is the sum of the cumulative stellar and hot gas fractions of Figures 2.2 and 3.2. The baryon fraction of L^* galaxies (open blue point) is gathered from Werk et al. (2014). The arrows indicate upper and lower-limits on the galaxy baryon fraction, while the error-bars represent the propagated error on the fraction, assuming independent uncertainties on the different galactic components (Section 2.4.2).

Groups and poor clusters are still slightly short of baryons within the virial radius

(shown by red points in Figure 3.5). However, there is no reason to assume that the gas density must cut-off suddenly at this relatively-arbitrary point. Direct observations (Planck Collaboration, 2013d) indicate that the gas fraction in massive clusters continues to increase beyond r_{vir} . Hence groups and poor clusters (where the baryon distribution is observed to be more extended than in massive clusters) should also have baryon reservoirs beyond this radius, which justifies our choice to extrapolate f_{gas} to $1.2r_{vir}$.

From galaxies to the most massive clusters, current observations are consistent with the entire cosmic baryon fraction being contained within the dark matter halo. Integrating out to r_{vir} and slightly beyond, there is no significant shortage of baryons, even in low-mass clusters and galactic systems, where previous estimates claimed a dramatic lack of baryonic mass. Considering the entire range of mass, there does not appear to be any strong correlation between enclosed baryon fraction with mass. The baryonic mass traces the dark matter mass in halos once their outer regions are included. Therefore, in response to the question “Where are the baryons in the universe”, we show that baryons have fallen into and stayed within dark matter halos, with some gas being expelled due to shock heating and other processes, and some colder gas infalling into galaxies. But the cosmic baryon fraction approximately traces the total mass distribution in the universe within and beyond the relevant r_{vir} .

Chapter 4

Discussion

4.1 Limitations and Observational Biases

Due to the sensitivity required to accurately measure the gas mass and total mass in clusters, our methods have included several assumptions (such as that the ICM is in hydrostatic equilibrium, and that the gas density slope is approximately constant from $\approx r_{500}$ or r_{200} to beyond r_{vir}) which require additional discussion. Here, we discuss theoretical and observational constraints on the magnitude of possible biases which we introduce by making these simplifications.

4.1.1 The Hydrostatic Mass Bias

As was highlighted throughout Chapter 2, there are several different ways to calculate the total mass of groups and clusters. One key characteristic of a mass estimation method is whether it relies on the assumption of hydrostatic equilibrium. The so-called “hydrostatic mass” (M_{HSE}) can be calculated by combining the gas density profile with either the temperature or pressure profile, a method ubiquitous in X-ray observations. Using mass-scaling relations (such as the Y_{SZ} - M_{500} relation) may also be sensitive to the assumption of HSE if the relation is calibrated against hydrostatic

masses. Masses which do not rely on the assumption of HSE are primarily derived from gravitational lensing.

Hydrostatic masses could be systematically biased, relative to the “true” mass (usually assumed to be the lensing mass, M_{WL}) if there are significant sources of non-thermal pressure in the ICM. Examples include kinetic bulk motions or magnetic fields. Hydrostatic equilibrium assumes that the gravitational force (the total mass) is offset by the pressure gradient, so assuming that only the gas pressure contributes can lead to a bias in the inferred mass.

The magnitude of the hydrostatic mass bias is of paramount importance to precision cosmology. Cosmological parameters (such as Ω_m) derived from *Planck* cluster counts and hydrostatic mass estimates disagree significantly from values derived directly from the CMB power spectrum, but a large hydrostatic mass bias ($b = 1 - M_{HSE}/M_{WL} \approx 0.3$) could relieve the observational tension (Gruen et al., 2013; von der Linden et al., 2014; Israel et al., 2014). Such a large bias on the total halo mass would also dramatically affect the gas fraction derived using hydrostatic masses, affecting its use as a cosmological probe (e.g., Grego et al., 2001; Ettori et al., 2009). As the majority of our f_{gas} measurements in clusters were measured relative to hydrostatic masses (with the exception of Umetsu et al. (2009)), our results are likewise sensitive to the hydrostatic bias.

Cosmological simulations are a major tool used to constrain this bias. The mass of simulated clusters can be compared to mock X-ray observations which assume hydrostatic equilibrium, determining the bias factor as a function of mass and overdensity. Simulations nearly unanimously indicate that the hydrostatic mass is biased low compared to the true halo mass ($b > 0$), a bias which increases towards the outskirts of clusters or in unrelaxed clusters, where merger disruptions and bulk flows become more significant. Different simulations and physical prescriptions place the bias anywhere from 5% (e.g., Lau et al., 2009; Meneghetti et al., 2010; Burns et al., 2010;

Nelson et al., 2012) to 20% (e.g., Arnaud et al., 2007; Nagai et al., 2007; Battaglia et al., 2013).

Observational constraints on the hydrostatic mass bias vary widely, however. Some weak lensing measurements of clusters suggest that hydrostatic X-ray or SZ masses are biased low by 10% (Andersson et al., 2011; High et al., 2012), and others indicate this bias could be as large as 20 – 30% (Arnaud et al., 2007; Ichikawa et al., 2013; von der Linden et al., 2014). Yet others find no significant difference between weak lensing masses and hydrostatic masses, with some hints that hydrostatic equilibrium assumptions may even *overestimate* the true mass in lower-mass clusters (Gruen et al., 2013; Israel et al., 2014). Figure 4.1, from Gruen et al. (2013), shows the agreement in their measured weak lensing and hydrostatic masses.

The issue of hydrostatic mass bias is far from solved. Due to the inconsistent observational and simulated constraints, it is unclear how large of a hydrostatic correction factor should be included in our measurements of the gas fraction, or if one is even necessary. A bias low in the hydrostatic mass would bias the gas fraction high, meaning that groups and clusters are slightly more deficient of baryons than we suggest. However, the shallow gas density slope suggests that, if the gas fraction is actually lower than observed, then integrating further beyond r_{vir} should recover the expected gas fraction. Our choice to avoid using a hydrostatic correction factor until this issue is clarified is slightly justified by the fact that one of our samples (U09) measures gas fraction against the weak lensing mass, and this fraction agrees well with gas fraction in similar clusters derived from the HSE assumption.

4.1.2 The Gas Clumping Bias

The primary means of deriving the gas density profile of clusters is from measurements of X-ray surface-brightness, which scales with the square of electron density. Due to this n^2 dependence, clumpy and overdense structures in the ICM will emit more

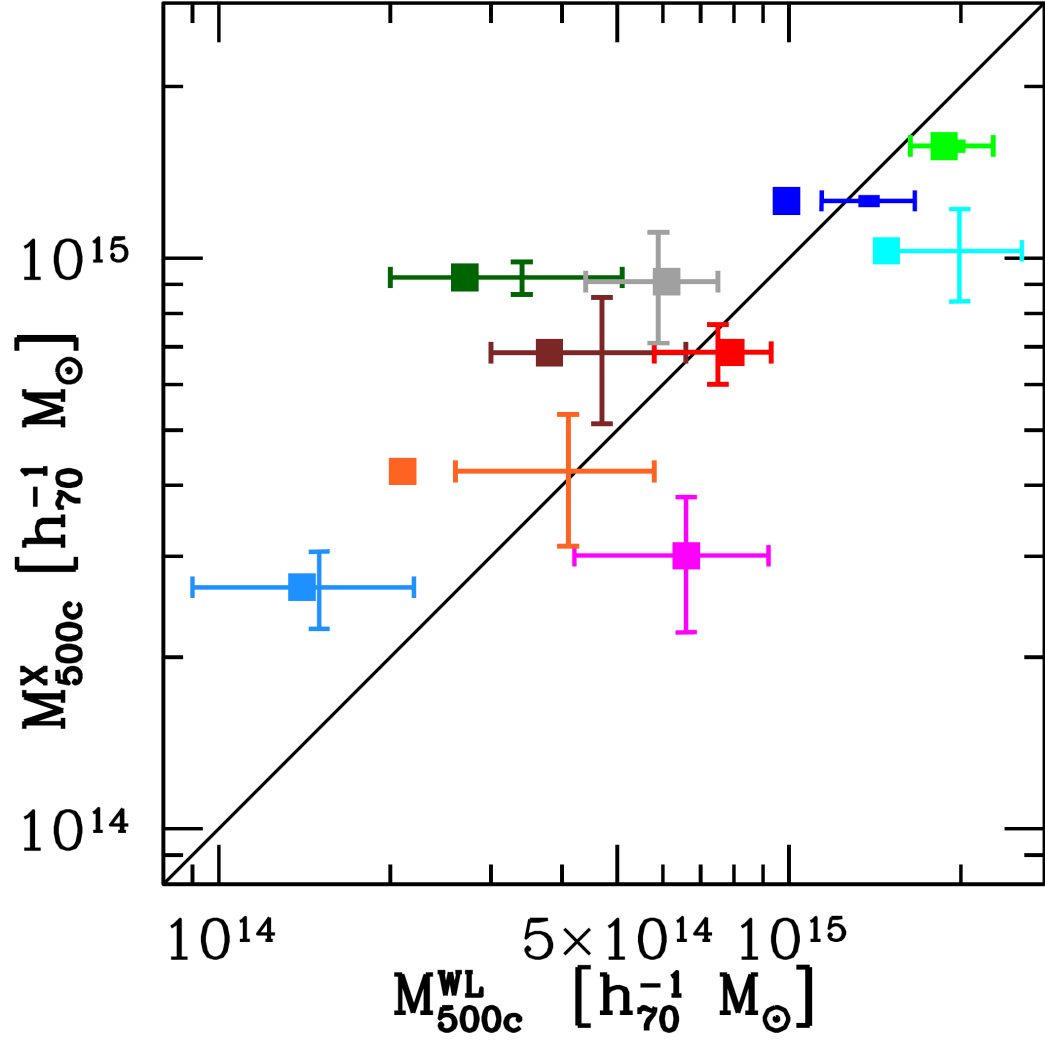


Figure 4.1: A comparison of weak lensing masses (M_{500c}^{WL}) and X-ray hydrostatic masses (M_{500c}^X) for SZ clusters, as presented in Gruen et al. (2013). Error bars indicate the best-fit “single-halo” fit, while the filled symbols include corrections to M^{WL} for other structures in the field of view. In tension with simulations, the authors find that hydrostatic masses are not systematically biased low relative to the weak lensing mass.

than their share of X-ray luminosity, biasing gas density measurements high. The magnitude of this bias depends on the smoothness of the ICM gas distribution, which can vary widely from cluster to cluster.

Simulations typically predict a clumping bias (overestimate of M_{gas}) of $\approx 10 - 15\%$ (Nagai & Lau, 2011; Battaglia et al., 2013), which increases in unrelaxed clusters and towards cluster outskirts, where recent interactions have a more significant dynamical effect. This could explain the large differences in measured gas fraction between CC and NCC clusters, although observations suggest that the level of clumpiness is overestimated in simulations, and that the average bias is below 10% (Eckert et al., 2013b). The majority of our cluster samples (with the exception of the PC13 sample) represent only relaxed (CC) clusters, so we do not include a clumping bias factor in our analysis. We also note that the P13 (Planck Collaboration, 2013d) and U09 (Umetsu et al., 2009) gas fractions are derived from SZ measurements, which do not suffer from this clumping bias, and agree well with our X-ray data sets.

4.1.3 Extrapolation of the Density Profile Slope

The choice to extrapolate the gas fraction to $1.2r_{vir}$ and then stop is arbitrary. Between r_{500} and r_{200} , observations disagree whether the slope remains roughly constant (Dai et al., 2010) or steepens by roughly 10% (Ettori & Balestra, 2009). Assuming the true evolution is somewhere in between, the gas density slope should not change appreciably relative to the total mass (NFW) profile, which steepens by about 4% within this range. Above r_{200} (where α_{gas} is measured), few accurate measurements of the gas density slope exist. Therefore, our simplified model that α_m and α_{gas} remain constant beyond r_{200} should roughly approximate the increase of f_{gas} with radius.

It is expected that the slope will eventually asymptote to match the total mass (NFW) profile (Umetsu et al., 2009; Battaglia et al., 2013), suggesting that, at large radius, α_{gas} will steepen more quickly than α_m . The point at which this occurs is

not well constrained, but it will taper the growth of f_{gas} , which should eventually reach a constant value. Planck Collaboration (2013d) finds that the gas fraction in stacked *Planck* clusters flattens out between 1 and $1.5r_{vir}$. We approximate this by extrapolating f_{gas} as constant above $1.2r_{vir}$. However, until temperature measurements beyond r_{500} improve, the true radius where the baryon fraction reaches a maximum will remain uncertain.

4.2 Comparison to Simulations

As discussed above, cosmological simulations have frequently been used to examine the magnitude of observational biases on measurements of cluster properties. Here we discuss the simulated cluster properties themselves, from the simulations of **Battaglia et al. (2013)**. We have discussed above that these simulations suggest that the assumption of HSE may bias our observed gas and baryon fractions high, and the true baryon fraction is lower by $\approx 10\%$. Here, we neglect these biases and compare the trends in their simulated gas and baryon fraction to our observations, having concluded earlier that the issue of mass bias is not yet settled.

The authors conducted a series of smoothed particle hydrodynamic (SPH) simulations with three different physical feedback prescriptions: 1) a “shock-heating” only method, 2) a method that also included radiative cooling and star formation/supernovae feedback, and 3) a prescription including AGN thermal feedback. The simulations produced (at $z = 0$) a sample of over 1000 clusters with $M_{200} > 7 \times 10^{13} M_{\odot}$, and 800 above $10^{14} M_{\odot}$.

Figure 4.2 shows the cumulative stellar, gas, and baryon fractions in the simulated clusters, as a function of mass (compare to our Figure 3.2). In the shock heating and radiative cooling models, the total baryon fraction within r_{200} is nearly the cosmic value in all clusters ranging from $10^{14} - 10^{15} M_{\odot}$. In the AGN feedback model,

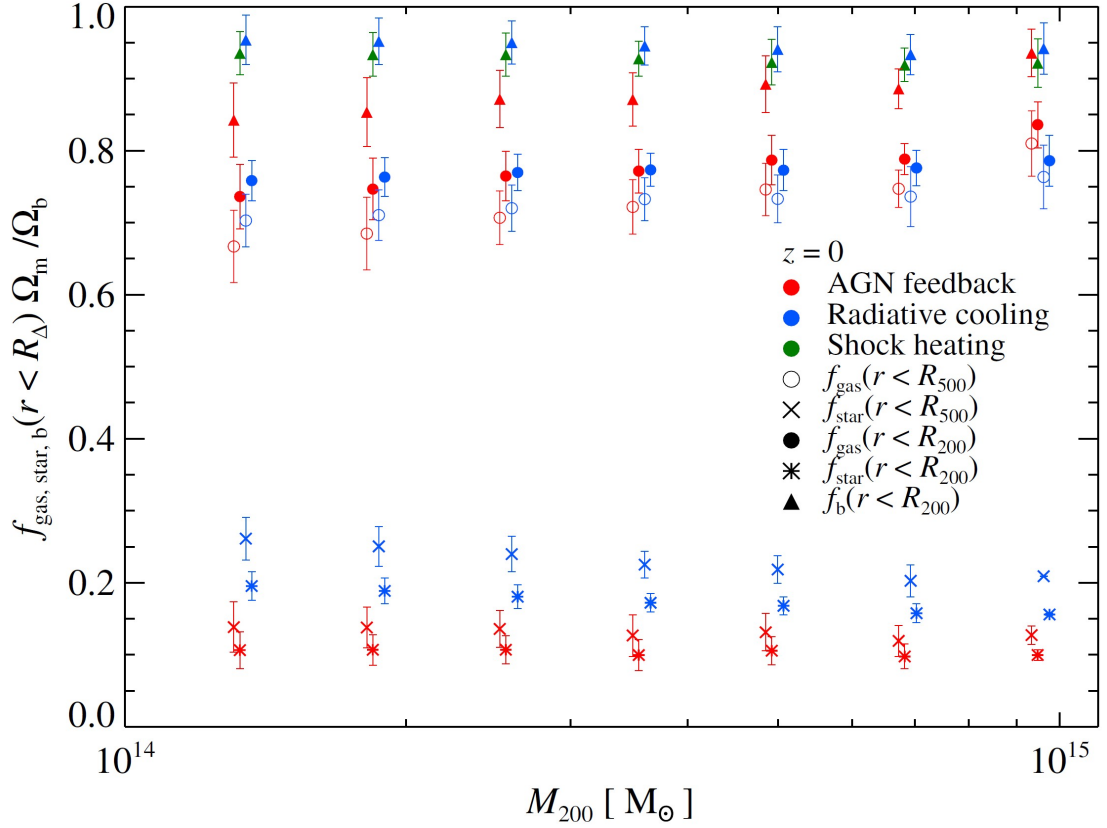


Figure 4.2: The gas, stellar, and baryon fraction (scaled by the cosmic baryon fraction) as a function of cluster mass from a series of simulations by Battaglia et al. (2013). The baryon fraction within r_{200} is close to the cosmic value for the entire mass range of $10^{14} - 10^{15} M_{\odot}$, except for in the AGN feedback model, where low-mass clusters have fewer baryons within r_{200} . These simulations are in agreement with our results, although the simulations predict a large hydrostatic mass bias (Section 4.1.1) that has yet to be confirmed observationally.

f_b decreases in smaller halos, due primarily to suppressed stellar mass production, although partly due to increased non-thermal pressure pushing the gas towards higher radius. These simulations are in agreement with our results that conclude the entire baryon fraction can be recovered in clusters of all mass ranges when accounting for cluster outskirts.

Figure 4.3 presents the radial distribution of the gas, stellar, and baryon fractions for clusters binned by mass. Only the results for the AGN feedback model are presented. The stellar fraction decreases significantly from the center of the clus-

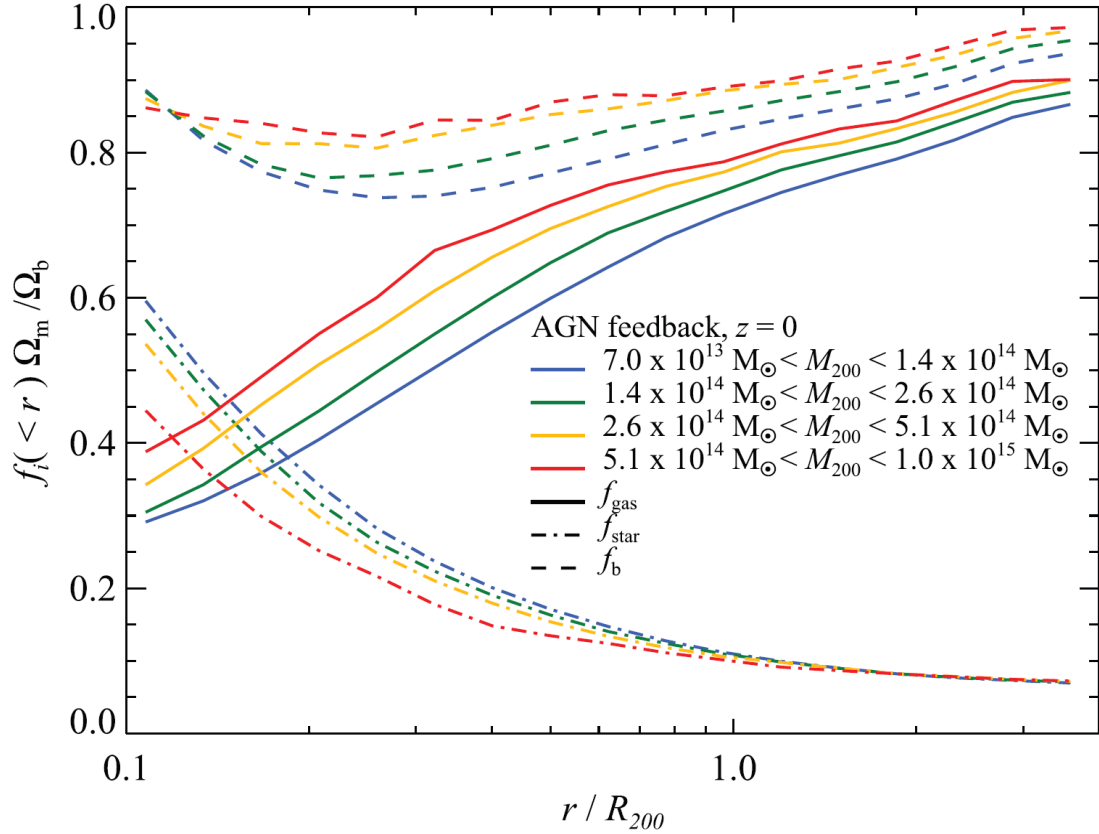


Figure 4.3: The gas, stellar, and baryon fraction distributions (scaled by the cosmic baryon fraction) as a function of radius in the simulations of Battaglia et al. (2013), binned in four parts by cluster mass. The stellar fraction and gas profiles match observations well, and the total baryon fraction approaches the cosmic value at high radius.

ters, with a higher stellar fraction in low-mass clusters for any given radius. In all mass bins, however, the stellar fraction asymptotically approaches a “cosmic” value of $\approx 7\%$ (relative to the baryon fraction). This behavior matches very well the stellar fraction profile measured by Bahcall & Kulier (2014), and the asymptotic level of the simulated stellar fraction is in excellent agreement with the observations (6% of the cosmic baryon fraction).

The gas fraction profile also matches our observed trends well. The gas fraction in the central regions of low mass clusters is significantly lower but increases more rapidly with radius than in high-mass clusters. The gas fraction in clusters of all mass

converges towards the same profile at high radius. Of particular interest, however, is that even at $r > 3r_{200}$ the gas fraction is still increasing steadily. If this represents the gas profile in real clusters (different feedback models have different behavior in the outskirts), then our assumption that the gas fraction remains constant above $1.2r_{vir}$ may need adjustment.

The overall baryon fraction increases from a minimum of 70 – 80% cosmic within $0.5r_{200}$ to $> 90\%$ outside the virial radius. The fact that the baryon fraction does not reach the cosmic fraction until very large radius ($> 4r_{200}$) differs slightly from our results, but this depends on the exact density profile being extrapolated. Improved observations of the gas profile slope beyond r_{200} will help constrain whether these simulations accurately predict how far beyond the virial radius the baryons are extended. Additionally, the simulations assume a cosmic baryon fraction of $f_b = 0.172$, higher than current observational estimates. The increased baryon abundance could lead to enhanced feedback effects, pushing baryons further from the cluster centers than actually observed. Simulations which match the current cosmological constraints would help clarify this issue.

Finally, in Figure 4.4, we show the redshift evolution in the gas fraction of the Battaglia et al. (2013) simulated clusters. Measured from the cluster centers to far beyond the virial radius, the gas fraction appears nearly constant with redshift at all radii. Measured from $z = 1.5 - 0$, this shows remarkable stability within the ICM over many gigayears, including the phase when the most massive clusters begin to form.

4.3 Implications

Having addressed the possible observational biases in our measurements and comparing our results to simulations, we address the global conclusions about the distribution

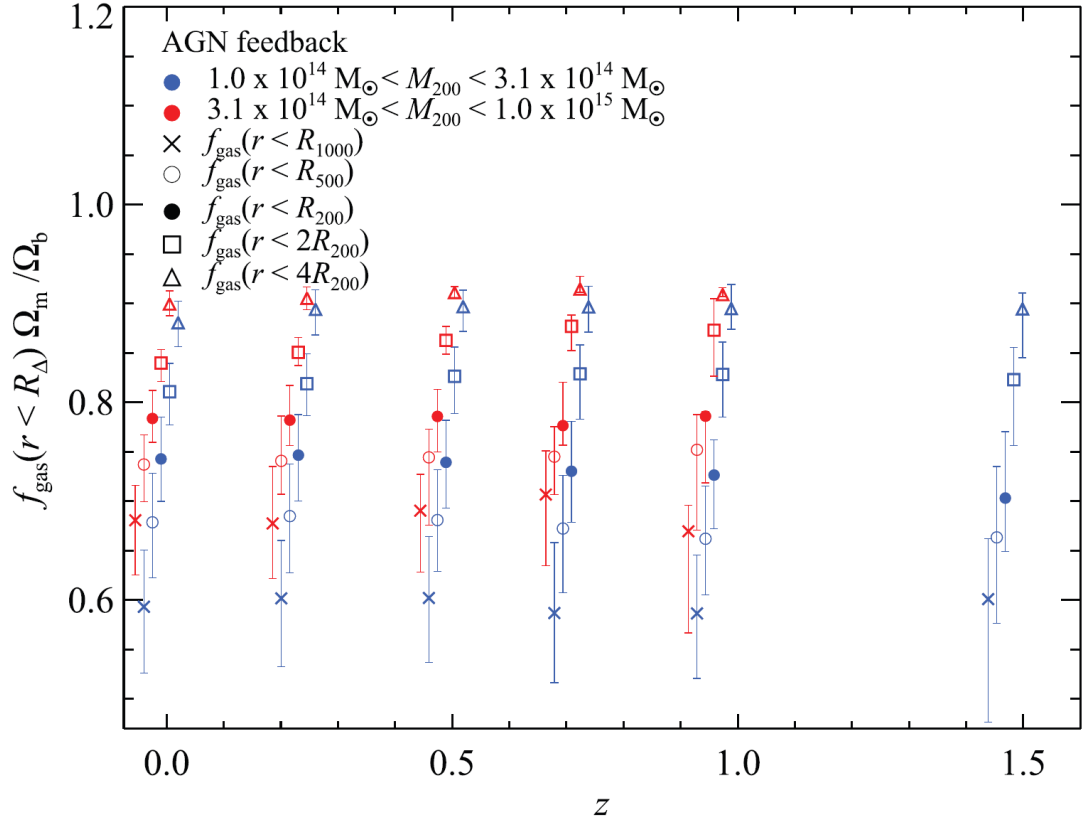


Figure 4.4: The gas fraction (scaled by the cosmic baryon fraction) within various radii, as a function of redshift, as measured by the simulations of Battaglia et al. (2013), and binned by mass. There is no significant redshift evolution of the gas fraction within any given radius, except possibly within $2r_{200}$, suggesting that measurements of the cluster baryon fraction should be fairly redshift independent back to $z \approx 1$, where massive clusters first begin to form.

of baryons that our results allow us to make. Understanding how baryons are distributed relative to dark matter and what relative forms they take in different halos will constrain how accurately baryons can be used as cosmological tools, and how much the baryon fraction changes and evolves from early cosmic times to today.

4.3.1 Deviations from Self-Similarity

Dark matter halos (both observationally and in simulations) are found to fit the NFW density profile, and hence are, roughly, “self-similar”. This means that all dark matter

halos have the same proportions and shapes, varying only by overall size. Assuming only gravitational collapse, physical properties of baryons in clusters (such as pressure and temperature) would be expected to obey “universal profiles”, once scaled to the appropriate halo size (e.g., Arnaud et al., 2010; Planck Collaboration, 2013d).

Although we have shown that the entire baryonic mass can be accounted for in halos ranging over three orders of magnitude in mass, the concentrations of gas and stellar fractions vary with halo mass. Pure self-similarity would suggest that the baryon fraction should reach the cosmic value at the same overdensity (such as r_{200} or r_{100}) regardless of halo mass. However, observations of the gas fraction (Section 3.1) and the stellar fraction (Bahcall & Kulier, 2014) in clusters indicate that the scale at which these fractions asymptote to the cosmic values decreases with cluster mass. Baryons in less massive halos are extended farther relative to their virial radii than in massive clusters, an observation which is supported by cosmological simulations (Battaglia et al., 2013).

Therefore, as expected, baryonic physics plays an important role in shaping the distribution of baryons on scales smaller than the virial radius in halos. Feedback effects (such as merger shocks, AGN feedback, and star formation) are able to push baryons further into the outskirts of small halos than in large halos, due to the decreased gravitational potential. However, as our results indicate, these feedback effects are not so powerful as to remove a substantial fraction of baryons from the halos altogether, and nearly the entire baryon fraction remains bound (or nearly bound) to dark matter halos.

4.3.2 The Contribution of Individual Galaxies to Clusters

Bahcall & Kulier (2014) found that the overall mass-to-light ratio of clusters matches closely the average mass-to-light ratio of individual galaxies (plus the added gas content), when normalized by the changing ratio of elliptical and spiral galaxies with

cluster radius (the “density-morphology relation”). This is consistent with the picture that the entire dark matter content of groups, clusters, and large-scale structure is comprised of the dark matter originally bound to galaxy halos, which fell into the clusters and was stripped to form the cluster halo. There is no reason, they argue, to assume that groups and clusters contain more dark matter (relative to light) than individual galaxy halos do (unlike as previously believed by e.g., Ostriker et al., 1974; Guo et al., 2010).

Our results further expand on this picture. The results described above suggest that the entire mass content of groups, clusters, and large-scale structure is comprised of the content of the infalling galaxies: the dark matter, stars, and gas. Combining the stellar mass of galaxies with observations of the multiphase CGM gas, Werk et al. (2014) demonstrated that large, $\sim L^*$ galaxies contain approximately the cosmic fraction of baryons within their ≈ 300 kpc halos, the same fraction observed within groups and clusters and expected to extend beyond into the large-scale structure. Individual $\sim L^*$ galaxies, falling into larger structures, may bring with them most of the dark matter and baryons which make up the larger systems. The consistency of the baryon fraction in galaxies and larger structures suggests that groups, clusters, and large-scale structure do not necessarily need a significant source of non-galactic baryons to explain the high abundances in their halos: the baryons could be comprised mostly of the baryonic mass once held in the halos of constituent galaxies. The ICM, therefore, could be mostly the stripped remains of galactic ISMs and CGMs, with the stellar disks remaining mostly as cluster galaxies, with a small amount being dispersed as the diffuse intracluster light (ICL).

Stars make up 15% of the baryons within the virial radius of $\sim L^*$ galaxies in the field, (Werk et al., 2014), in good agreement with the $\approx 15\%$ stellar fraction of baryons within r_{vir} of groups (Bahcall & Kulier, 2014). This agreement further suggests that the total stellar mass of groups could be made up of the contribution

of individual L^* galaxies which fell into groups. As the baryon fraction of galaxies is also consistent with that of groups (within the virial radius), most of the dark matter, gas, and stellar fraction of groups could come from the constituent galaxies.

The baryon content of massive clusters, however, is made up of a smaller fraction of stars, only $\approx 6\%$ within r_{vir} . This may suggest that galaxies only make up $\sim 6/15 = 40\%$ of the stellar (and baryonic) mass of clusters, and additional (non-galactic) gas and dark matter may have fallen into rich clusters to decrease the cluster stellar fraction. Another possible solution is that galaxies which fell into massive clusters did not form as many stars, with the hot environment of the cluster quenching star formation in the constituent galaxies. We also note that the average total mass of L^* galaxies assumed by Bahcall & Kulier (2014) ($\approx 3 \times 10^{12} M_\odot$) and Werk et al. (2014) ($\approx 1.6 \times 10^{12} M_\odot$) differ by a non-negligible margin, and could explain the difference in their stellar fractions. Further analysis is required to more accurately measure the stellar fraction in L^* galaxies, groups, and clusters, but we appear close to being able to constrain the contribution of galaxies to the total stellar and baryonic mass of groups and clusters.

4.3.3 Where are the Baryons?

Our results show that the entire expected baryon content of dark matter halos can be detected or inferred using current observations. While the gaseous component of the baryons is more extended than the dark matter, they are still bound to their host halos, and there is no significant problem of baryons missing from halos. Therefore, the answer to the question, “Where are the baryons in dark matter halos?” is answered simply as: they are found in the halos, distributed in various combinations between the central regions and the diffuse outskirts.

The size and frequency of virialized halos define the overall structure of matter in the universe. Because baryons populate in nearly equal abundances galactic, group,

and cluster halos, on large scales they represent excellent tracers of the overall dark matter distribution and structure. A relevant physical scale seems to be the halo virial radius: this scale separates the regimes where baryons do/do not trace the dark matter. On scales smaller than the virial radius, baryons are under-abundant, relative to their cosmic fraction, due to heating and other baryonic physics; this shortage is dependent on the overall mass of the halo. However, averaging on scales larger than r_{vir} , baryons match the dark matter distribution of the cosmos at a nearly constant fraction.

During the earliest phases of structure formation baryons and dark matter fell (in the cosmic fraction) into the newly forming gravitational potentials. Whether baryons remained in these dark matter halos at this cosmic fraction, or if baryonic physics expelled a large fraction of the baryons from the system, has been unknown until now. Our results suggest that virialized systems, from galaxies to groups, clusters, and even large-scale structure, all retain approximately the cosmic fraction of baryons. Heating and other feedback effects have broadened the baryon distribution, so that baryons are further extended into the outskirts of halos than dark matter, but they remain in the expected cosmic fraction within the potential. This picture further suggests, as originally proposed by Bahcall & Kulier (2014), that the makeup of groups, clusters, and large-scale structure may be nearly entirely dominated by the contributions of individual $\sim L^*$ galaxies: their dark matter and baryons, gas, and stars.

Chapter 5

Summary and Conclusions

In this thesis, we present a synthesis of observational constraints on the distribution and abundance of baryons in dark matter halos over a wide range of masses. Baryons, while only 16% of the total mass in the universe, are the most easily detectable form of matter and are incredibly important tools in understanding and observing the formation of structure in the universe. Previous observations suggest halos are deficient in baryons relative to the cosmic fraction, a discrepancy known as the “Missing Baryon Problem”. We trace the baryon distribution in halos from galactic scales ($M_{vir} = 10^{12} M_{\odot}$) to groups ($M_{vir} = 10^{13} M_{\odot}$), and clusters ($M_{vir} = 10^{14} - 10^{15} M_{\odot}$) to address the missing baryon problem, to understand how baryons trace the distribution of total mass, and to obtain a global picture of the distribution of baryons relative to dark matter in the universe.

Our group and cluster gas mass data is comprised of a collection of X-ray and SZ measurements of the gas density, temperature, and pressure profiles in the ICM. The total mass is derived either through the assumption of hydrostatic equilibrium or by using weak lensing. When the gas fraction is not measured to the virial radius, we extrapolate the observed gas fraction using gas density profile slopes appropriate to the given halo mass or ICM temperature (Rasheed et al., 2011). Our galaxy

cluster data comes from a compilation by Werk et al. (2014), and includes absorption measurements of the multiphase CGM, stellar masses, and ISM masses from HI surveys.

Our main results are as follows:

1. Although the gas fraction within r_{500} in groups and clusters is significantly lower than the cosmic baryon fraction, the gas distribution is more extended than the dark matter distribution due to shock heating and other baryonic processes, such that the gas fraction increases significantly when integrated to the cluster outskirts.
2. The gaseous ICM is more extended in low-mass systems, explaining why the gas fraction is observed to be particularly low within r_{500} in these halos. The gas fraction rises more steeply with radius in groups and poor clusters than in massive clusters, and our extrapolations predict that the gas fraction of all groups and clusters is consistent with cosmic fraction near r_{vir} .
3. The cluster stellar fraction at any given radius is higher in groups and poor clusters, due to the dominance of the BCG, although in groups and clusters of all sizes the fraction asymptotically approaches the “cosmic” stellar fraction 0.01 ± 0.004 at high enough radius.
4. Observational constraints on the gas content of galactic halos find the cool CGM can account for 25 – 50% of the total cosmic baryonic mass fraction. Adding the baryons located in the stellar disk, ISM, and multiphase CGM result in a galactic baryon fraction for $\sim L^*$ galaxies that is nearly consistent with the cosmic fraction within the viral radius of ~ 300 kpc around L^* galaxies.
5. Combining the observed baryonic components of galaxies, groups, and clusters, we show that dark matter halos may contain the cosmic fraction of baryons

within approximately the virial radius, across three orders of magnitude in total mass.

6. The baryonic distribution in halos is not entirely self-similar. Baryons in less-massive halos are pushed farther into the outskirts of the shallow gravitational well by feedback mechanisms, not reaching the cosmic fraction until higher radii. The abundance of different baryonic components (particularly stellar mass and gas) also changes somewhat with cluster mass.
7. The consistent baryon fraction in galactic and cluster halos suggests that dark matter and baryonic masses in groups and clusters could be composed entirely of matter originally in galactic halos which fell into the larger systems. The dark matter of galactic potentials could have been stripped to form the group and cluster halo, and the galactic CGM gas, stripped and heated when falling into the potential, could be sufficient to explain the gas found in the ICM of groups and clusters. The stellar fraction of individual L^* galaxies agrees with the stellar fraction of groups, and while clusters have a lower stellar fraction, this could be due to a suppression of star formation in cluster galaxies rather than requiring a large additional source of gas and dark matter to fall into clusters.
8. The baryon distribution of the universe traces the dark matter distribution reasonably well, with no need for additional unseen or unbound reservoirs of baryons from halos. Averaged over scales larger than the virial radius, baryons map the total structure of the universe, and the baryonic mass of clusters is an effective proxy for the total mass.
9. The combination of these observations suggests that baryons, which originally fell with the cosmic fraction into halos, remain in the systems with approximately the same cosmic fraction. Despite baryon processes such as heating,

infall, and feedback, which play an important role in expanding the hot gas distribution relative to the dark matter, the baryons remain largely within the dark matter halos of galaxies, groups, and clusters.

Improvements in the precision of our results will come from better constraints of the ICM temperature profile at large radii (in groups and clusters) and of the mass in the warm CGM phase (in galaxies). Additionally, further weak lensing calibrations are required to constrain the magnitude of the hydrostatic equilibrium bias on the total cluster mass.

Our results suggest new ways to place constraints on the cosmology of the universe. Dark matter is notoriously difficult to detect or measure accurately, with the only direct method being with gravitational lensing. Baryons, however, emit or absorb radiation in a variety of measurable ways. The knowledge that baryons trace the underlying dark matter profile allows the use of baryon mass distributions to constrain the abundance and masses of halos (e.g., Ettori et al., 2009). Until recently, baryons were thought to have been expelled from the gravitational potentials of galaxies, groups, and clusters. Our results show that baryons which fall into these systems remain within their potentials, and can serve as useful tools to study the evolution of halos, the cosmology of the low-redshift universe, and the growth of large-scale structure.

Bibliography

- Afshordi, N., Lin, Y.-T., Nagai, D., & Sanderson, A. J. R. 2007, *Monthly Notices of the Royal Astronomical Society*, 378, 293
- Anderson, M. E., Bregman, J. N., & Dai, X. 2013, *The Astrophysical Journal*, 762, 106
- Andersson, K., et al. 2011, *The Astrophysical Journal*, 738, 48
- Arnaud, M., Pointecouteau, E., & Pratt, G. W. 2007, *Astronomy and Astrophysics*, 474, L37
- Arnaud, M., Pratt, G. W., Piffaretti, R., Böhringer, H., Croston, J. H., & Pointecouteau, E. 2010, *Astronomy and Astrophysics*, 517, A92
- Bahcall, J. N., & Spitzer, L. J. 1969, *The Astrophysical Journal*, 156, L63
- Bahcall, N. A., & Kulier, A. 2014, *Monthly Notices of the Royal Astronomical Society*, 439, 2505
- Battaglia, N., Bond, J. R., Pfrommer, C., & Sievers, J. L. 2013, *The Astrophysical Journal*, 777, 123
- Behroozi, P. S., Conroy, C., & Wechsler, R. H. 2010, *The Astrophysical Journal*, 717, 379
- Bennett, C. L., et al. 2003, *The Astrophysical Journal Supplement Series*, 148, 1
- Bergeron, J. 1985, *Astronomy and Astrophysics*, 155, L8-L11 (1986)
- Bialek, J. J., Evrard, A. E., & Mohr, J. J. 2001, *The Astrophysical Journal*, 555, 597
- Bode, P., Ostriker, J. P., & Vikhlinin, A. 2009, *The Astrophysical Journal*, 700, 989
- Bonamente, M., Lieu, R., Mittaz, J. P. D., Kaastra, J. S., & Nevalainen, J. 2005, *The Astrophysical Journal*, 629, 192

- Booth, C. M., Schaye, J., Delgado, J. D., & Dalla Vecchia, C. 2012, *Monthly Notices of the Royal Astronomical Society*, 420, 1053
- Burns, J. O., Skillman, S. W., & O'Shea, B. W. 2010, *The Astrophysical Journal*, 721, 1105
- Cen, R., Miralda-Escude, J., Ostriker, J. P., & Rauch, M. 1994, *The Astrophysical Journal*, 437, L9
- Cen, R., & Ostriker, J. P. 1999, *The Astrophysical Journal*, 514, 1
- Chen, H.-W., Helsby, J. E., Gauthier, J.-R., Shethman, S. A., Thompson, I. B., & Tinker, J. L. 2010, *The Astrophysical Journal*, 714, 1521
- Dai, X., Bregman, J. N., Kochanek, C. S., & Rasia, E. 2010, *The Astrophysical Journal*, 719, 119
- Dave, R., Hernquist, L., Katz, N., & Weinberg, D. H. 1999, *The Astrophysical Journal*, 511, 521
- Dodelson, S. 2003, *Modern Cosmology* (San Diego: Academic Press)
- D'Odorico, S., & Savaglio, S. 1991, *Quasar Absorption Lines*, *Proceedings of the ESO Mini-Workshop held 20-21 February, 1991*. Organized by P.A. Shaver, E.J. Wampler and A.M. Wolfe., p.51
- Dunkley, J., et al. 2009, *The Astrophysical Journal Supplement Series*, 180, 306
- Durrer, R. 2008, *The Cosmic Microwave Background* (New York, NY: Cambridge University Press)
- Eckert, D., Ettori, S., Molendi, S., Vazza, F., & Paltani, S. 2013a, *Astronomy & Astrophysics*, 551, A23
- Eckert, D., Ettori, S., Molendi, S., Vazza, F., Roncarelli, M., Gastaldello, F., & Rossetti, M. 2013b, e-print arXiv:1310.8389
- Eckert, D., Molendi, S., Vazza, F., Ettori, S., & Paltani, S. 2013c, *Astronomy & Astrophysics*, 551, A22
- Eckert, D., et al. 2012, *Astronomy & Astrophysics*, 541, A57
- Eke, V. R., Cole, S., & Frenk, C. S. 1996, *M.N.R.A.S.*, 282, 263-280 (1996)
- Ettori, S., & Balestra, I. 2009, *Astronomy and Astrophysics*, 496, 343
- Ettori, S., Morandi, A., Tozzi, P., Balestra, I., Borgani, S., Rosati, P., Lovisari, L., & Terenziani, F. 2009, *Astronomy and Astrophysics*, 501, 61

- Giardini, S., et al. 2009, *The Astrophysical Journal*, 703, 982
- Grego, L., Carlstrom, J. E., Reese, E. D., Holder, G. P., Holzapfel, W. L., Joy, M. K., Mohr, J. J., & Patel, S. 2001, *The Astrophysical Journal*, 552, 2
- Gruen, D., et al. 2013, eprint arXiv:1310.6744, 36
- Guo, Q., White, S., Li, C., & Boylan-Kolchin, M. 2010, *Monthly Notices of the Royal Astronomical Society*, 11
- Gupta, A., Mathur, S., Krongold, Y., Nicastro, F., & Galeazzi, M. 2012, *The Astrophysical Journal*, 756, L8
- High, F. W., et al. 2012, *The Astrophysical Journal*, 758, 68
- Hinshaw, G., et al. 2013, *The Astrophysical Journal Supplement Series*, 208, 19
- Ichikawa, K., et al. 2013, *The Astrophysical Journal*, 766, 90
- Iocco, F., Mangano, G., Miele, G., Pisanti, O., & Serpico, P. D. 2009, *Physics Reports*, 472, 1
- Israel, H., Reiprich, T. H., Erben, T., Massey, R. J., Sarazin, C. L., Schneider, P., & Vikhlinin, A. 2014, e-print arXiv:1402.3267, 2
- Kirkman, D., Tytler, D., Suzuki, N., OMeara, J. M., & Lubin, D. 2003, *The Astrophysical Journal Supplement Series*, 149, 1
- Komatsu, E., & Seljak, U. 2001, *Monthly Notices of the Royal Astronomical Society*, 327, 1353
- Lanzetta, K. M., Bowen, D. B., Tytler, D., & Webb, J. K. 1995, *The Astrophysical Journal*, 442, 538
- Lau, E. T., Kravtsov, A. V., & Nagai, D. 2009, *The Astrophysical Journal*, 705, 1129
- Linsky, J. L., Diplas, A., Wood, B. E., Brown, A., Ayres, T. R., & Savage, B. D. 1995, *The Astrophysical Journal*, 451, 335
- Linsky, J. L., et al. 1993, *The Astrophysical Journal*, 402, 694
- Mandelbaum, R., Seljak, U., & Hirata, C. M. 2008, *Journal of Cosmology and Astroparticle Physics*, 2008, 006

- Martin, A. M., Papastergis, E., Giovanelli, R., Haynes, M. P., Springob, C. M., & Stierwalt, S. 2010, *The Astrophysical Journal*, 723, 1359
- McCarthy, I. G., Bower, R. G., & Balogh, M. L. 2007, *Monthly Notices of the Royal Astronomical Society*, 377, 1457
- McGaugh, S. S., Schombert, J. M., de Blok, W. J. G., & Zagursky, M. J. 2010, *The Astrophysical Journal*, 708, L14
- Meléndez, J., & Ramírez, I. 2004, *The Astrophysical Journal*, 615, L33
- Meneghetti, M., Rasia, E., Merten, J., Bellagamba, F., Ettori, S., Mazzotta, P., Dolag, K., & Marri, S. 2010, *Astronomy and Astrophysics*, 514, A93
- Metzler, C. A., & Evrard, A. E. 1994, *The Astrophysical Journal*, 437, 564
- Moster, B. P., Somerville, R. S., Maubetsch, C., van den Bosch, F. C., Macciò, A. V., Naab, T., & Oser, L. 2010, *The Astrophysical Journal*, 710, 903
- Mukhanov, V. 2005, *Physical Foundations of Cosmology* (New York, NY: Cambridge University Press)
- Nagai, D., & Lau, E. T. 2011, *The Astrophysical Journal*, 731, L10
- Nagai, D., Vikhlinin, A., & Kravtsov, A. V. 2007, *The Astrophysical Journal*, 655, 98
- Navarro, J. F., Frenk, C. S., & White, S. D. M. 1996, *The Astrophysical Journal*, 462, 563
- Nelson, K., Rudd, D. H., Shaw, L., & Nagai, D. 2012, *The Astrophysical Journal*, 751, 121
- Niemann, H. B., et al. 1996, *Science*, 272, 846
- Oppenheimer, B. D., Davé, R., Katz, N., Kollmeier, J. A., & Weinberg, D. H. 2012, *Monthly Notices of the Royal Astronomical Society*, 420, 829
- Oppenheimer, B. D., Davé, R., Kereš, D., Fardal, M., Katz, N., Kollmeier, J. A., & Weinberg, D. H. 2010, *Monthly Notices of the Royal Astronomical Society*, 406, 2325
- Ostriker, J. P., Peebles, P. J. E., & Yahil, A. 1974, *The Astrophysical Journal*, 193, L1

- Peeples, M. S., Werk, J. K., Tumlinson, J., Oppenheimer, B. D., Prochaska, J. X., Katz, N., & Weinberg, D. H. 2014, *The Astrophysical Journal*, 786, 54
- Planck Collaboration. 2011, *Astronomy & Astrophysics*, 536, A11
- . 2013a, e-print arXiv:1303.5062
- . 2013b, eprint arXiv:1303.5076
- . 2013c, *Astronomy & Astrophysics*, 558, C2
- . 2013d, *Astronomy & Astrophysics*, 550, A131
- Prochaska, J. X., Weiner, B., Chen, H.-W., Mulchaey, J., & Cooksey, K. 2011, *The Astrophysical Journal*, 740, 91
- Rasheed, B., Bahcall, N., & Bode, P. 2011, *Proceedings of the National Academy of Sciences of the United States of America*, 108, 3487
- Ryden, B. 2003, *Introduction to Cosmology* (San Francisco: Addison Wesley)
- Sargent, W. L. W., Young, P. J., Boksenberg, A., & Tytler, D. 1980, *The Astrophysical Journal Supplement Series*, 42, 41
- Sheldon, E. S., et al. 2009a, *The Astrophysical Journal*, 703, 2217
- . 2009b, *The Astrophysical Journal*, 703, 2232
- Spergel, D., Flauger, R., & Hlozek, R. 2013, eprint arXiv:1312.3313
- Steidel, C. C., Erb, D. K., Shapley, A. E., Pettini, M., Reddy, N., Bogosavljević, M., Rudie, G. C., & Rakic, O. 2010, *The Astrophysical Journal*, 717, 289
- Steigman, G. 2006, *International Journal of Modern Physics E*, 15, 1
- Sun, M., Voit, G. M., Donahue, M., Jones, C., Forman, W., & Vikhlinin, A. 2009, *The Astrophysical Journal*, 693, 1142
- Sunyaev, R. A., & Zeldovich, Y. B. 1972, *Comments on Astrophysics and Space Physics*, Vol. 4, p.173
- Suzuki, T. K., Yoshii, Y., & Beers, T. C. 2000, *The Astrophysical Journal*, 540, 99

- Takizawa, M., & Mineshige, S. 1998, *The Astrophysical Journal*, 499, 82
- Thom, C., et al. 2012, *The Astrophysical Journal*, 758, L41
- Tumlinson, J., et al. 2011, *Science* (New York, N.Y.), 334, 948
- Tytler, D., Fan, X. M., & Burles, S. 1996, *Nature*, 381, 207
- Umetsu, K., et al. 2009, *The Astrophysical Journal*, 694, 1643
- Vikhlinin, A., Kravtsov, A., Forman, W., Jones, C., Markevitch, M., Murray, S. S., & Van Speybroeck, L. 2006, *The Astrophysical Journal*, 640, 691
- von der Linden, A., et al. 2014, *ArXiv e-prints*
- Weinberg, S. 2008, *Cosmology* (New York, NY: Oxford University Press)
- Werk, J. K., Prochaska, J. X., Thom, C., Tumlinson, J., Tripp, T. M., O'Meara, J. M., & Peeples, M. S. 2013, *The Astrophysical Journal Supplement Series*, 204, 17
- Werk, J. K., et al. 2014, e-print arXiv:1403.0947, 19
- Zhu, G., & Ménard, B. 2013, *The Astrophysical Journal*, 773, 16